Magnetic Phase Transitions in Dysprosium Orthoferrite $DyFeO_3$ — Reconstruction of the Magnetic Domain Structure During Transitions

K. Piotrowski*

Instytute of Physics, Polish Academy of Sciences, al. Lotników 32/46, PL-02668 Warsaw

Received: 14.07.2025 & Accepted: 15.10.2025

Doi: 10.12693/APhysPolA.148.185 *e-mail: piotr@ifpan.edu.pl

Due to their potential applications in spintronics, as well as their ferroelectric, magnetocaloric, and lasing properties, rare-earth orthoferrites ($RFeO_3$) have recently seen a renewed surge of scientific interest. In line with this trend, the present work provides an overview of research on magnetic phase transitions in dysprosium orthoferrite ($DyFeO_3$). Both spontaneous and field-induced transitions are investigated based on the evolution of the magnetic domain structure, induced by temperature variations and external magnetic fields applied in various configurations with respect to the crystallographic axes of the sample. Phenomenological models of these transitions are presented and analyzed, leading to the construction of phase diagrams that are compared with experimental results.

topics: magnetic order, magnetic phase transition, magnetic domain structures

1. Introduction

Rare-earth orthoferrites ($RFeO_3$), which crystallize in perovskite orthorhombic (space group D_{2h}^{16}–Pbnm), exhibit a rich variety of magnetic phase transitions [1–4] that manifest as changes in physical parameters measurable during the course of these transitions. Given this, the observation of the magnetic domain structure in materials undergoing such transitions is a particularly suitable approach for analyzing magnetic phenomena. The existing domain structure reflects the current magnetic state of the sample, as it results from the internal magnetic interactions (dependent on the relation between the anisotropic Dzyaloshinskii–Moriya antisymmetric exchange and isotropic exchange interactions) present within the material. It is also influenced by internal stress, defects, and external factors such as temperature and applied magnetic fields. These external parameters affect the magnetic interactions, and thus, by studying the domain structure under their influence, one can probe and analyze the mechanisms responsible for the resulting magnetic state of the sample.

The motivation for this study stems from a resurgence of interest in rare-earth orthoferrites $RFeO_3$ as a class of materials. This renewed attention is driven by their diverse physical properties, including ferroelectricity, magnetocaloric effects, lasing capabilities, and magnetic phase transitions, as well as their characteristic fast spin dynamics.

$DyFeO_3$ is a material with the Dzyaloshinskii–Moriya interaction, which introduces noncollinearities in the spin structure and offers intriguing opportunities for the investigation of such heavily debated topics of condensed matter physics as the emergence of helicoidal spin textures, skyrmions, and multiferroicity. $DyFeO_3$ is treated as an archetypal antiferromagnet. Recent works [5–12] investigating phase transitions in orthoferrites, including $DyFeO_3$, highlight their significance for advancing the understanding of magnetoelectric effects in $RFeO_3$ systems. These findings point to the potential utility of field-controlled phase transitions in spintronic devices.

A thorough understanding of magnetic phase transitions and the corresponding phase diagrams is essential for the strategic application of magnetic materials in spintronics and related magnetic technologies.

2. Studies on the properties of dysprosium orthoferrite

This paper presents a review and synthesis of studies on magnetic phase transitions in dysprosium orthoferrite ($DyFeO_3$). These transitions were identified and interpreted through the visualization and analysis of changes and reconstructions within the magnetic domain structure, particularly in the vicinity of the transition points and throughout

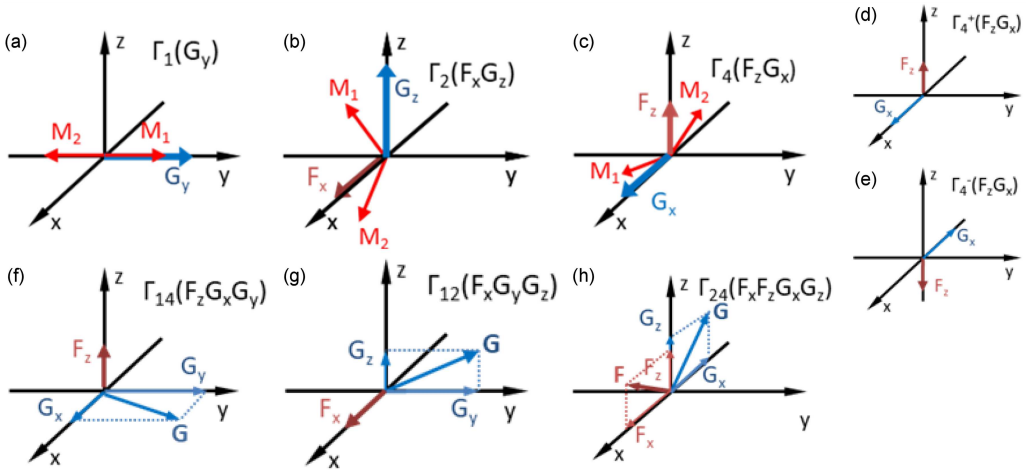

Fig. 1. The ferromagnetic $\boldsymbol{F}$ and antiferromagnetic $\boldsymbol{G}$ vectors in the two-sublattice model shown in the basic orthoferrite phases: (a) $\Gamma_1(G_y)$, (b) $\Gamma_2(F_xG_z)$, (c) $\Gamma_4(F_zG_x)$. The $\boldsymbol{F}$ and $\boldsymbol{G}$ vectors shown in the $\Gamma_4(F_zG_x)$ phase in (d) Γ_4^+ and (e) Γ_4^- domains. The $\boldsymbol{F}$ and $\boldsymbol{G}$ vectors in the (f) $\Gamma_{14}(F_zG_xG_y)$, (g) $\Gamma_{12}(F_xG_yG_z)$, (h) $\Gamma_{24}(F_xF_zG_xG_z)$ phases induced by the magnetic field (x, y, and z axis orientations correspond to crystallographic a, b, and c axes, respectively).

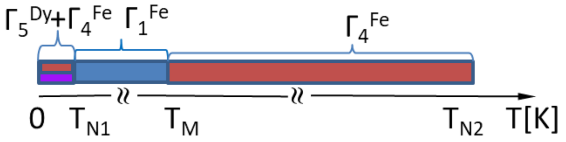

Fig. 2. Schematically presented magnetic ranges, related to Fe and Dy ordering, in $DyFeO_3$ versus temperature. Temperatures are $T_{N1} \approx 3.7$ K, $T_M \approx 51.6$ K, $T_{N2} \approx 645$ K. Magnetic phase notations are consistent with those introduced by Bertaut [13], see also Fig. 1.

their progression. The classification of the observed magnetic phases follows the notation introduced by Bertaut [13]. In this classification, symmetry-allowed spin configurations in orthoferrites are described by the Γ_i ($i = 1, 2, \ldots 8$) irreducible representations of a $Pbnm$ (D_{2h}^{16}) space group. Spin configurations in orthoferrites can be denoted by the same symbols, i.e., Γ_i. In this work, in the two magnetic sublattices ($\boldsymbol{M}_1, \boldsymbol{M}_2$) approach, only the components of the vectors $\boldsymbol{F} = \boldsymbol{M}_1 + \boldsymbol{M}_2$ and $\boldsymbol{G} = \boldsymbol{M}_1 - \boldsymbol{M}_2$ will be used to describe the configuration Γ_i. The canted configurations involving both Γ_i and Γ_j are denoted by Γ_{ij}. In the Γ_{ij} configuration basis, vector components of both irreducible representations of Γ_i and Γ_j are nonzero.

The configurations of ferromagnetic $\boldsymbol{F}$ and antiferromagnetic $\boldsymbol{G}$ vectors in the two-sublattice model in antiferromagnetic state Γ_1 and weak ferromagnetic states Γ_2 and Γ_4 for orthoferrites without an external magnetic field are presented in Fig. 1.

Dysprosium orthoferrite ($DyFeO_3$) was selected to represent a particularly promising material from the orthoferrite family for observing domain structures under the influence of a magnetic field. This choice is supported by the presence of spontaneous magnetic phase transitions — transitions driven solely by changes in temperature. These include three distinct transitions, listed here (and schematically presented in Fig. 2) in order of decreasing temperature:

(i) The paramagnetic to weak ferromagnetic transition occurring at the Néel temperature T_{N2};

(ii) The weak ferromagnetic to antiferromagnetic transition at the so-called Morin temperature T_M;

(iii) A second antiferromagnetic to weak ferromagnetic transition observed at pumped helium temperatures, associated with magnetic ordering of the dysprosium sublattice, T_{N1}.

The most extensively studied magnetic phase transition in $DyFeO_3$ is the spontaneous transition from the antiferromagnetic state $\Gamma_1(G_y)$ to the weak ferromagnetic state $\Gamma_4(F_zG_x)$, which can also be induced by an external magnetic field applied parallel to either the c or b axis of the crystal. The $DyFeO_3$ samples used in these studies were prepared as thin plates of 35–40 μm thickness, with the c axis oriented perpendicular to the surface. All samples were etched in orthophosphoric acid to remove the surface layer deformed by mechanical processing. The experimental approach relied on optical observation and photographic recording of the domain structure evolution during the magnetic phase transition, utilizing the magneto–optical Faraday effect. Linearly polarized light was directed perpendicularly to the sample surface. Infrared filters were introduced into the optical path to minimize local heating effects from the light beam.

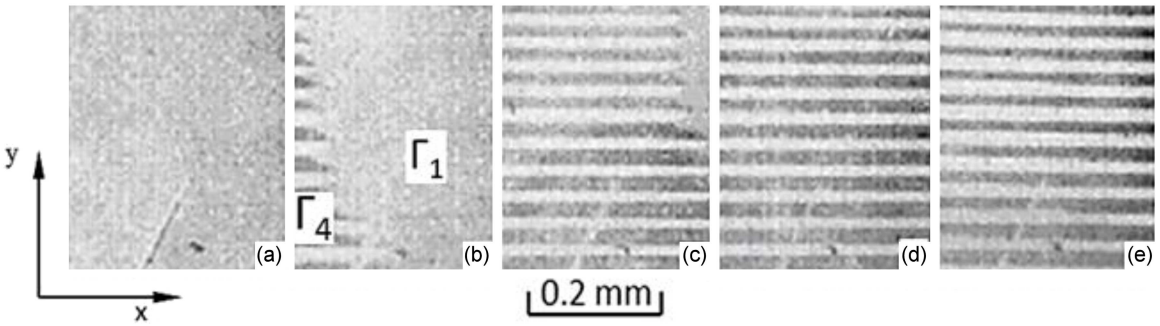

Fig. 3. Magnetic domain structure during field-induced evolution of the magnetic ordering from $\Gamma_1(G_y)$ to $\Gamma_4(F_zG_x)$ phase in $DyFeO_3$ single crystal (cut perpendicular to crystallographic c axis; measuring temperature $T = 7$ K; x, y, and z axis orientations correspond to crystallographic a, b, and c axes, respectively) in an external magnetic field $\boldsymbol{H} \parallel \boldsymbol{b}$ (with $H_z = 0$). The values of the magnetic field H_y [Oe] are: (a) 6520, (b) 6720, (c) 6810, (d) 7030, (e) 9500. Image adapted from [17].

Optical investigations of the domain structure during the $\Gamma_1 \leftrightarrow \Gamma_4$ transition, induced by temperature changes, have been reported in [14]. Studies of the same transition, but triggered by a magnetic field parallel to the c axis, are presented in [15, 16]. Analysis of the domain behavior during the transition indicates that when an external magnetic field is applied parallel to the b axis (but within a temperature range where the antiferromagnetic Γ_1 state is stable), a spin-flop type phase transition should occur and be observable. A key experimental requirement is achieving a sufficiently strong external field to initiate the transition. For this purpose, superconducting coils are particularly suitable, especially if they are constructed to allow real-time observation and recording of the domain structure and its evolution as a function of temperature and applied magnetic field. The results of experimental investigations into the spin-flop magnetic phase transition have been reported in [17].

3. Studies of magnetic ordering changes driven by an external magnetic field

3.1. Magnetic field applied along the crystallographic b and c axes

The measurements discussed here were conducted at 7 K, i.e., the temperature at which the $\Gamma_1(G_y)$ antiferromagnetic state is the spontaneous ground state of $DyFeO_3$. The external magnetic field $(\boldsymbol{H} \parallel \boldsymbol{b}) = H_y$ was generated using a superconducting magnet, while the magnetic field $(\boldsymbol{H} \parallel \boldsymbol{c}) = H_z$ was produced using air-cooled conventional coils.

The application of $\boldsymbol{H} \parallel \boldsymbol{b}$ and real-time observation (by using the Faraday effect sensitive to the z component of the magnetization) enabled the determination of the field-induced magnetic ordering changes to the $\Gamma_4(F_zG_x)$ weak ferromagnetic state. While increasing the magnetic field, the $\Gamma_1(G_y)$ phase changes into the $\Gamma_4(F_zG_x)$ phase consisting of two magnetization configurations, i.e., domains with magnetization in line with the z axis or against it (they are $\Gamma_4^+(F_z^+G_x)$ or $\Gamma_4^-(F_z^-G_x)$, respectively). At temperature $T = 7$ K, at which $\Gamma_1(G_y) \rightarrow \Gamma_4(F_zG_x)$ occurs, this critical magnetic field is approximately $(H_y)_{sf} = 6.6$ kOe [17].

Increasing the magnetic field $\boldsymbol{H} \parallel \boldsymbol{b}$ beyond $(H_y)_{sf}$ progressively expands the volume fraction of the Γ_4 weak ferromagnetic phase within the sample, until it occupies the entire volume of the sample. Nucleation sites for the Γ_4 phase typically correspond to defects, sample edges, or existing domain walls within the Γ_1 antiferromagnetic phase. Due to the rectangular plate geometry of the samples, the spatial emergence of regions exhibiting phase coexistence ($\Gamma_1 + \Gamma_4$) is not easily predictable. In the case illustrated in Fig. 3, a scratch on the sample served as the nucleation center. The experimentally determined range of magnetic field values $\boldsymbol{H} \parallel \boldsymbol{b}$ over which phase coexistence is observed spans approximately 500 Oe.

Figure 3 clearly shows that the field-induced Γ_4 phase consists of weakly ferromagnetic domains, further subdividing into subphases — in the figure, the subphases are represented as alternating bright and dark stripes. Once the transition is complete, the domain structure within the Γ_4 phase remains largely unchanged up to fields of about $\boldsymbol{H} \parallel \boldsymbol{b} \approx 10$ kOe. However, full magnetic saturation of the sample can be readily achieved by applying an additional magnetic field along the c axis, with saturation occurring at $\boldsymbol{H} \parallel \boldsymbol{c} \approx 260$ Oe.

The observed $\Gamma_1 \rightarrow \Gamma_4$ transition is reversible. Upon decreasing the field $\boldsymbol{H} \parallel \boldsymbol{b}$, the system undergoes a reverse phase transition, i.e., $\Gamma_4 \rightarrow \Gamma_1$.

Detailed studies of the $\Gamma_1 \leftrightarrow \Gamma_4$ transition induced by an external magnetic field composed of two vector components $\boldsymbol{H} \parallel \boldsymbol{b}$ and $\boldsymbol{H} \parallel \boldsymbol{c}$ enabled the construction of the phase diagram at 7 K, shown in Fig. 4. The domain evolution presented in Fig. 3 corresponds to the specific case of $H_z = 0$

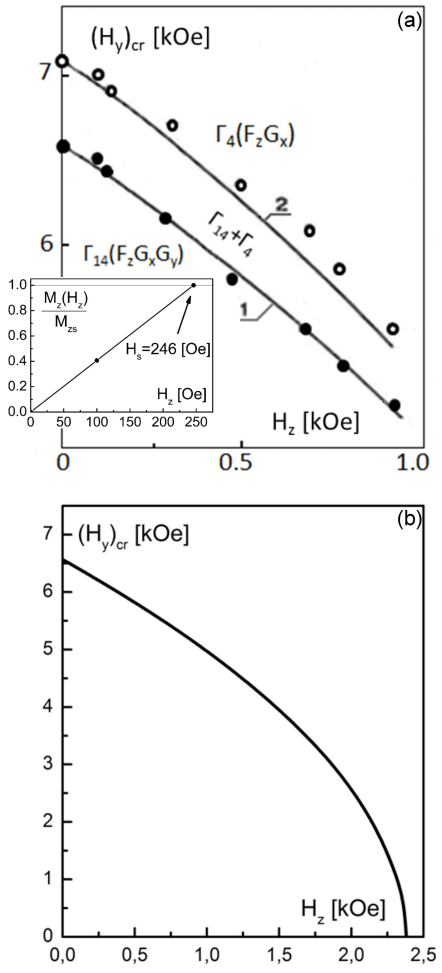

Fig. 4. The critical field $(H_y)_{cr}$ versus $\boldsymbol{H} \parallel \boldsymbol{c}$ for the phase transition $\Gamma_{14}(F_zG_xG_y) \leftrightarrow \Gamma_4(F_zG_x)$. (a) Solid lines 1 and 2 represent theoretical calculations, while filled and open circles correspond to experimental points marking the onset and completion of the phase transition, respectively. The experiment was performed at $T = 7$ K. Figure adapted from [17]. In the inset, the normalized magnetization $M(H_z)$ is shown, given by the relation of the difference between the Γ_4^+ and Γ_4^- domain widths divided by the sum of the Γ_4^+ and Γ_4^- widths in the Γ_4 phase. The saturation field H_s was estimated to be $\simeq 246$ Oe. (b) Diagram plotted using (2) in the full range of magnetic field corresponds to line 1 in panel (a).

(a simple transformation $\Gamma_1 \rightarrow \Gamma_4$). When both fields H_y and H_z are applied, the situation becomes more complicated for the transitions Γ_1 to Γ_{14} and finally to Γ_4.

When both magnetic fields $\boldsymbol{H} \parallel \boldsymbol{c}$ and $\boldsymbol{H} \parallel \boldsymbol{b}$ are simultaneously applied to the sample (at $T = 7$ K), the field $\boldsymbol{H} \parallel \boldsymbol{c}$ induces a rotation of the magnetization of the Fe^{3+} sublattice from the crystallographic b axis toward the a axis (phase $\Gamma_1(G_y)$ is transformed to $\Gamma_{14}(F_zG_xG_y)$ phase). In this case, the magnetic phase transition induced by a strong field $\boldsymbol{H} \parallel \boldsymbol{b}$ corresponds to a transition from phase $\Gamma_{14}(F_zG_xG_y)$ to phase $\Gamma_4(F_zG_x)$ (schematically written as $\Gamma_{14} \rightarrow \Gamma_4$) in the next step. The nature of this transition differs depending on whether the value of $\boldsymbol{H} \parallel \boldsymbol{c}$ is below or above the saturation field H_s of the domain structure in phase Γ_4. Therefore, the behavior of the magnetic domain structure should be analyzed and examined for both H_z field regimes.

Magnetic ordering was discussed considering the thermodynamic potential expression for phase $\Gamma_{14}(F_zG_xG_y)$ [17], given by the following formula

$$\Phi = \left[K_2^{(ab)} + (1+\eta_y)^2 \frac{H_y^2}{2A}\right] \sin^2(\varphi) - M_z H_z \cos(\varphi), \tag{1}$$

where:

$K_2^{(ab)}$ — anisotropy constant in the crystallographic ab plane,

η_y — enhancement coefficient (reflecting the influence of Dy^{3+} ions),

A — exchange constant,

M_z — magnetization of $DyFeO_3$ in the Γ_4 phase,

φ — angle between the antiferromagnetic vector and the crystallographic a axis.

The critical field $(H_y)_{cr}$, determined from the above expression for the thermodynamic potential, at which the phase transition $\Gamma_{14} \rightarrow \Gamma_4$ occurs, is described by the following relation

$$(H_y)_{cr} = (H_y)_{sf} \sqrt{1 + \frac{M_z H_z}{2K_2^{(ab)}}}, \tag{2}$$

where $(H_y)_{sf}$ is the value of the magnetic field H_y at which the spin-flop transition occurs when $H_z = 0$, and $(H_y)_{sf}$ is related to the material parameters by the following expression

$$(H_y)_{sf} = \frac{1}{1+\eta_y} \sqrt{2\left|K_2^{ab}\right| A}. \tag{3}$$

Line 1 presented in Fig. 4 was determined based on (2) for the ratio of magnetization to anisotropy constant $M_z/(2K_2^{(ab)}) = -4.2 \times 10^{-4}$ Oe^{-1}.

The relation $2K_2^{(ab)}/M_z$, having a value of -2381 Oe, defines the anisotropy field.

Line 2 was constructed using (2) adding 500 Oe estimated from experiment. Furthermore, (2) was also used to construct the phase diagram in Fig. 4b.

3.1.1. Case $H_z < H_s$

Let us consider the $H_z < H_s$ case (where H_s is the saturation field for the domain types $\Gamma_4^+(F_z^+G_x)$ and $\Gamma_4^-(F_z^-G_x)$ in phase Γ_4). In this case, phase $\Gamma_4(G_xF_z^+)$ appears within the Γ_{14} phase upon the application of the magnetic field H_y, forming a striped domain structure inclined at 16° to

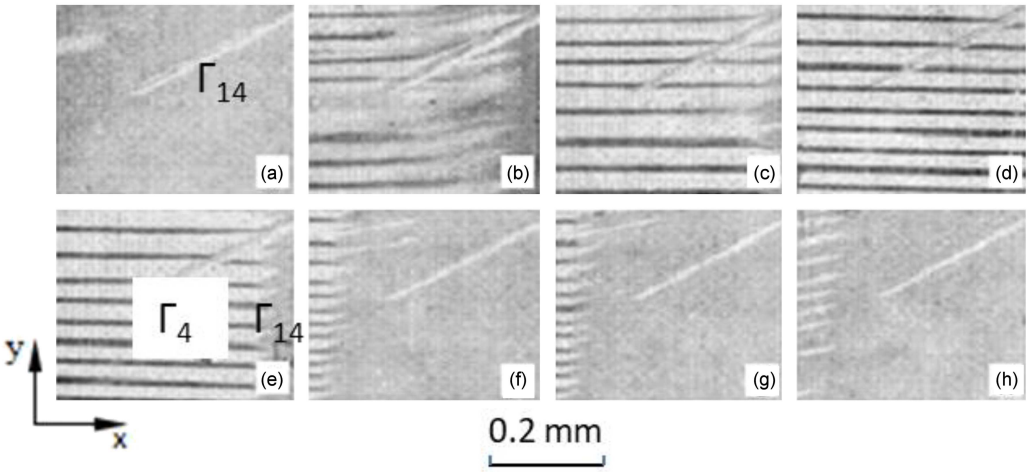

Fig. 5. Magnetic domain structure evolution induced by a magnetic field $H \parallel \boldsymbol{b}$ (where $H_z = 100$ Oe; cut perpendicular to the crystallographic c axis; and x, y, and z axis orientations correspond to crystallographic a, b, and c axes, respectively) at $T = 7$ K in a $DyFeO_3$ single crystal in the antiferromagnetic state. The values of the magnetic field H_y [Oe] are: (a) 6450, (b) 6580, (c) 6660, (d) 6850, (e) 6570, (f) 6490, (g) 6450, (h) 6430. Image adapted from [17].

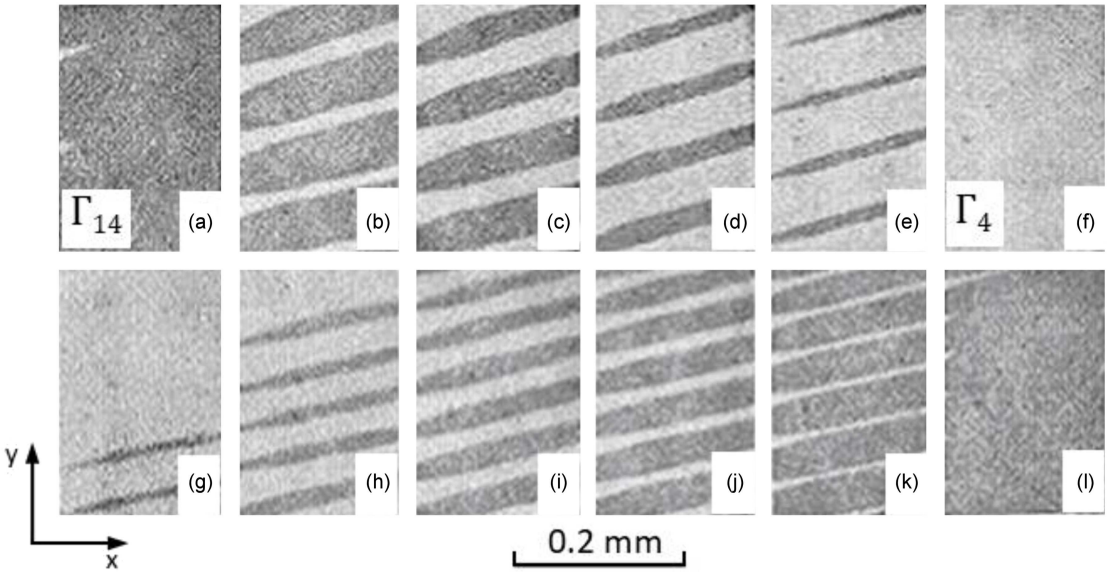

Fig. 6. Magnetic domain structure evolution induced by a magnetic field $\boldsymbol{H} \parallel \boldsymbol{b}$ (where $H_z = 450$ Oe; cut perpendicular to the crystallographic c axis; and x, y, and z axis orientations correspond to crystallographic a, b, and c axes, respectively) at $T = 7$ K in a $DyFeO_3$ single crystal in the antiferromagnetic state. The values of the magnetic field H_y [Oe] are: (a) 5980, (b) 6110, (c) 6170, (d) 6220, (e) 6280, (f) 6330, (g) 6250, (h) 6190, (i) 6150, (j) 6100, (k) 6040, (l) 5990. Image adapted from [17].

the crystallographic a axis. Further increase of the field H_y leads to the emergence of a third magnetic phase $\Gamma_4(G_xF_z^-)$. The resulting weakly ferromagnetic Γ_4 region is then subdivided into stripe domains consisting of $\Gamma_4^+(F_z^+G_x)$ and $\Gamma_4^-(F_z^-G_x)$, with domain walls aligned parallel to the crystallographic a axis. This scenario of the magnetic phase transition is illustrated in Fig. 5.

An interesting observation from the experiments on the magnetic phase transition $\Gamma_1 \rightarrow \Gamma_4$ induced by the magnetic field H_y is that within the emerging weakly ferromagnetic Γ_4 phase, no changes were observed in the period of the weakly ferromagnetic domains as a function of the applied H_y field. This behavior of the domain structure provides insights into the configuration of domain walls in the resulting domain pattern. The only plausible explanation for the absence of period changes in the domain structure of phase Γ_4 is that the magnetization rotation within the domain wall occurs in the crystallographic ac plane at the temperatures used in the experiments. When compared with theoretical

predictions [18], this experimental result indicates that the magnetic field H_y does not influence magnetization rotation occurring in the ac plane. It also suggests that this type of magnetization change cannot occur in a 90° domain wall, since in such walls, as opposed to 180° walls, the magnetization rotates within the crystallographic ab plane.

3.1.2. Case $H_z > H_s$

In the $H_z > H_s$ case, the sample enters a mixed state composed of phase domains representing Γ_{14} and $\Gamma_4(F_z^+G_x)$, where the '+' sign indicates magnetization aligned with the direction of the field H_z. The observed magnetic domains exhibit regular shapes, and their domain walls form an angle of approximately 16° with respect to the crystallographic a axis. This behavior of the magnetic phase transition is illustrated in Fig. 6. The figure presents images of the domain structure evolution during the transition induced by the external magnetic field H_y (from phase Γ_{14} to the saturated Γ_4 phase, and the reverse transition from Γ_4 back to Γ_{14}) under the condition $H_z > H_s$.

A separate body of research on magnetic phase transitions induced by external magnetic fields $\boldsymbol{H} \parallel \boldsymbol{b}$ in $DyFeO_3$ orthoferrite concerns studies conducted at the lowest temperature ranges, starting from 1.6 K. Investigations of the domain structure [19] have shown that in the temperature range $1.6 < T < 6$ K, and in a magnetic field $\boldsymbol{H} \parallel \boldsymbol{b}$, phase transitions $\Gamma_1 \rightarrow \Gamma_{1234} \rightarrow \Gamma_4$ occur. First, from the antiferromagnetic phase (present in zero field) to a field-induced spatially modulated phase $\Gamma_1(G_y) \rightarrow \Gamma_{1234}(F_xF_yF_zG_xG_yG_z)$, in which the ferromagnetic and antiferromagnetic vectors are oriented in three-dimensional space — this is a second-order phase transition. Second, the transition $\Gamma_{1234} \rightarrow \Gamma_4$ from this spatially modulated phase to the weak ferromagnetic phase Γ_4 is a first-order phase transition.

In [19], an H–T phase diagram of the investigated transitions is presented, along with a discussion of the obtained results. That work is further developed in [20, 21], which provide detailed results of domain structure observations and measurements of the magnetic moment during transitions at the lowest temperatures, enabling a complete characterization of the magnetic phases present.

3.2. Magnetic field applied along the crystallographic a axis. Weak ferromagnet–weak ferromagnet phase transition near Morin temperature (T_M)

According to the results presented in [3], the application of a magnetic field $\boldsymbol{H} \parallel \boldsymbol{a}$ to an orthoferrite sample induces a magnetic phase transition $\Gamma_4(F_zG_x) \rightarrow \Gamma_2(F_xG_z)$. In the weakly ferromagnetic state $\Gamma_2(F_xG_z)$ (Fig. 1b), the vectors $\boldsymbol{G}$ and $\boldsymbol{F}$ are oriented along the crystallographic c and a axes, respectively. The observed spin reorientation proceeds via a continuous rotation of the $\boldsymbol{G}$ and $\boldsymbol{F}$ vectors within the crystallographic ac plane, passing through an intermediate phase $\Gamma_{24}(F_xF_zG_xG_z)$, and is completed as a second-order phase transition $\Gamma_{24}(F_xF_zG_xG_z) \rightarrow \Gamma_2(F_xG_z)$ [3].

This interpretation of the phase transition, based on known experimental data, remained valid until the publication of direct experimental observations of the transition in $DyFeO_3$ orthoferrite, reported in [22]. The results presented there confirmed theoretical predictions [23, 24] that the transition may proceed through a sequence of transitions: $\Gamma_4(F_zG_x) \rightarrow \Gamma_{24}(F_xF_zG_xG_z) \rightarrow \Gamma_{12}(F_xG_yG_z) \rightarrow \Gamma_2(F_xG_z)$, where phase Γ_{12} represents a spin configuration in which the $\boldsymbol{F}$ vector is parallel to the crystallographic a axis, while the antiferromagnetic vector $\boldsymbol{G}$ lies within the crystallographic bc plane. Within this sequence, the $\Gamma_{24} \rightarrow \Gamma_{12}$ transition is a first-order phase transition.

The emergence of this transition results from competing interactions among anisotropy, antisymmetric Dzyaloshinskii–Moriya interaction, and isotropic exchange interactions. The existence of this magnetic phase transition ($\Gamma_{24} \rightarrow \Gamma_{12}$) in orthoferrites was experimentally demonstrated for the first time in [22].

Figure 7 presents representative images of magnetic phases configuration during the $\Gamma_{24}(F_xF_zG_xG_z)$ [transformed from $\Gamma_4(F_zG_x)$] $\rightarrow \Gamma_{12}(F_xG_yG_z)$ transition (at $T > T_M$) induced by an external magnetic field applied along the crystallographic a axis ($\boldsymbol{H} \parallel \boldsymbol{a}$) (without the field, the sample is in the $\Gamma_4(F_zG_x)$ phase). From images, one can deduce:

- The opposite direction of ferromagnetic vector component at neighboring stripe domains in the Γ_{24} phase, more precisely, $\Gamma_{24}^+(F_xF_z^+G_xG_z) + \Gamma_{24}^-(F_xF_z^-G_xG_z)$ from $\Gamma_4(F_z^+G_x) + \Gamma_4(F_z^-G_x)$;
- The lack of z component of magnetization in Γ_{12}, which is expected from $\Gamma_{12}(F_xG_yG_z)$. The corresponding experimental phase diagram in the H–T plane is shown in Fig. 8. Experimental points in the diagram correspond to the condition in which both Γ_{24} and Γ_{12} phases coexist within the field of view of the domain structure and occupy equal surface areas.

In [22], an expression for the thermodynamic potential was presented, which served as the basis for analyzing the observed sequence of magnetic phase transitions. This analysis allowed the determination of the trajectory of the $\boldsymbol{G}$ vector during the transition, as well as the derivation of formulas describing the critical magnetic fields of individual

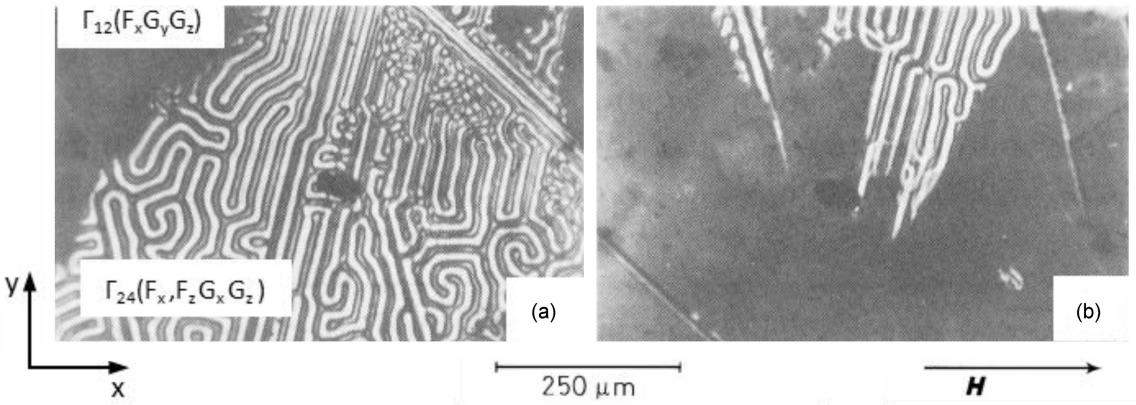

Fig. 7. Representative images of the domain structure in a $DyFeO_3$ sample (cut perpendicular to the crystallographic c axis; x, y, and z axis orientations correspond to crystallographic axes a, b, and c, respectively) during the $\Gamma_{24}(F_x, F_z, G_x, G_z)$ [transformed from $\Gamma_4(F_zG_x)$] $\rightarrow \Gamma_{12}(F_xG_yG_z)$ transition. Values of the external magnetic field $\boldsymbol{H} \parallel \boldsymbol{a}$ correspond to the phase coexistence range [22]. Here, $(T - T_{\mathrm{M}}) = 0.6$ K, $T_{\mathrm{M}} = 51.6$ K, (a) $H_x = 6.3$ kOe, (b) $H_x = 6.7$ kOe. Image adapted from [22].

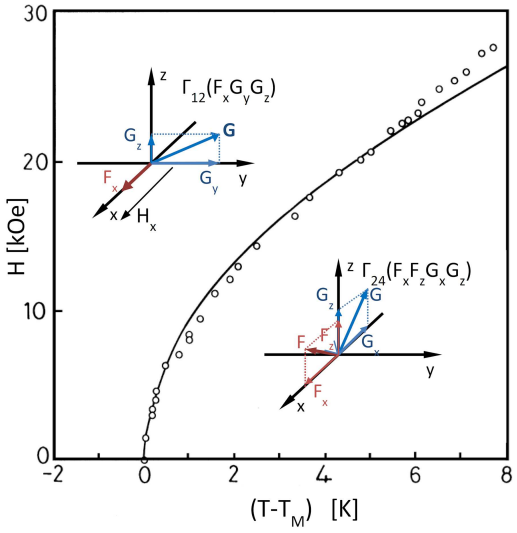

Fig. 8. Experimentally determined phase diagram in the H–T plane for the transition $\Gamma_{24} \rightarrow \Gamma_{12}$ in $DyFeO_3$. The orientations of the ferromagnetic and antiferromagnetic vectors relative to the crystallographic directions are shown for both phases [22] (x, y, and z axis orientations correspond to crystallographic a, b, and c axes, respectively). Figure adapted from [22].

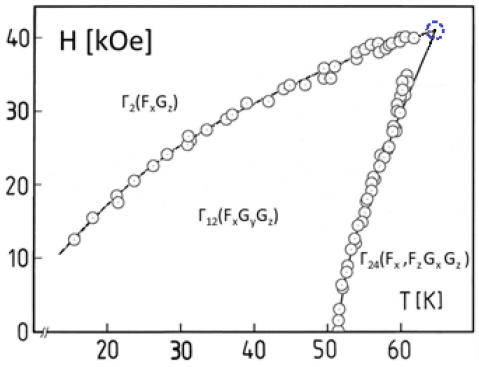

Fig. 9. Phase diagram H–T of $DyFeO_3$ showing the magnetic phases $\Gamma_2(F_xG_z)$, $\Gamma_{12}(F_xG_yG_z)$, $\Gamma_{24}(F_xF_zG_yG_z)$ and the tricritical point (H_{cr}, T_{cr}) distinguished by a large dashed circle. The magnetic field was applied along the a axis. Figure adapted from [26].

transitions in the sequence, with relation to the magnetic parameters of $DyFeO_3$.

The conclusion of the study, based on both experimental data and theoretical considerations, was that the $\Gamma_{24} \leftrightarrow \Gamma_{12}$ transition in $DyFeO_3$ at temperatures $T > T_{\mathrm{M}}$ is a first-order phase transition, during which the spin system undergoes a discontinuous reorientation from the crystallographic ac plane to the bc plane. The analysis presented in [12] further indicates that the phase transition line $\Gamma_{24} \leftrightarrow \Gamma_{12}$ from the transition sequence $\Gamma_4 \rightarrow \Gamma_{24} \rightarrow \Gamma_{12} \rightarrow \Gamma_2$ merges with the phase transition line $\Gamma_{12} \leftrightarrow \Gamma_2$ at a critical point with coordinates (H_{cr}, T_{cr}) on the H–T phase diagram (see Fig. 9).

Reference [22] provides the experimental values of H_{cr} and T_{cr}. It was also shown that for temperatures $T > T_{cr}$, spin reorientation occurs as a continuous rotation within the crystallographic ac plane, ending with a second-order phase transition $\Gamma_{24} \rightarrow \Gamma_2$ consistent with the interpretation accepted prior to the publication of [22].

Studies of the magnetic phase transition in $DyFeO_3$ near the Morin point were presented in [17]. There, the authors introduced a phenomenological model and reported magneto–optical observations of a new type of magnetic transition between magnetic phases $\Gamma'_{124} \rightarrow \Gamma''_{124}$, occurring at temperatures close to T_{M}. This transition is a

first-order magnetic phase transition induced by an external magnetic field applied within the crystallographic ab plane of the $DyFeO_3$ crystal. In the Γ_{124} phase, the vector $\boldsymbol{G}$ is not localized in one of the ab, ac, or bc planes, and all its components G_x, G_y, and G_z are non-zero. The canted configuration for this phase is denoted by $\Gamma_{124}(F_xF_zG_xG_yG_z)$.

In [25], the H–T phase diagram for this transition, obtained for various orientations of the magnetic field $\boldsymbol{H}$ within the ab plane of the studied samples, was presented. Excellent agreement between the experimental data and the calculated transition curves based on the proposed model validated the adopted theoretical description. Magneto–optical measurements of a sample with the a axis perpendicular to the surface additionally enabled determination of the critical point parameters ($H_{cr} \cong 35$ kOe, $T_{cr} \cong 54.5$ K) for the $\Gamma_{24} \rightarrow \Gamma_{12}$ transition described in [22].

The study [25] was also the first in a series of works focusing on domain structure investigations in oblique magnetic fields.

The magnetic phase diagram at larger temperature and field ranges was studied in [26], see Fig. 9.

The results obtained in [22] inspired further exploration of the discussed sequence of magnetic transitions across a broader temperature range, with special attention to the $\Gamma_{24} \rightarrow \Gamma_{12}$ transition. Magneto–optical measurements of Faraday rotation and birefringence, along with direct observation and imaging of the domain structure, allowed for the construction of a phase diagram presented in Fig. 9, as reported in [26]. This diagram clearly reveals the existence of a tricritical point. Reference [26] presents detailed information about the experimental setup, along with a comprehensive theoretical analysis of the studied transitions. A precise examination of the phase diagram near the tricritical point, as well as the specifics of the measurement technique, are discussed in [27].

4. Magnetic phase transitions in $DyFeO_3$ in oblique magnetic fields (fields with orientations deviated from crystallographic axes)

The analysis of magnetic phase transitions in rare-earth orthoferrites in oblique magnetic fields has been the subject of numerous studies, including [25, 28–31]. However, it is important to note that investigations of phase transitions in oblique fields were practically nonexistent until the publication of [25]. The justification for undertaking such studies lies in the fact that oblique magnetic fields (i.e., those deviating from the symmetry axes of the crystal) lead to the emergence of new low-symmetry magnetic phases, alterations in the nature of phase transitions, and the appearance of critical points in magnetic phase diagrams.

Studying phase transitions in oblique fields through the observation of domain structures enables the analysis of the transition process from a non-periodic two-phase state to a periodic one, depending on the orientation of the external magnetic field. Dysprosium orthoferrite ($DyFeO_3$) is an especially suitable material for such investigations due to the presence of first-order magnetic phase transitions within specific temperature ranges and for certain magnetic field orientations. These transitions occur when magnetic fields are applied along the rhombic axes of the crystal.

Magnetic phase transitions involving spin reorientation and magnetically inhomogeneous states in $DyFeO_3$ have been studied in oblique magnetic fields oriented within the crystallographic ab, ac, and bc planes. These studies were conducted across a wide range of magnetic field orientation angles relative to the crystallographic directions within the specified planes. As a result, they have revealed consistent patterns in the formation and reconstruction of the two-phase domain structure that arises during first-order phase transitions in oblique fields. A significant outcome of these investigations is the identification of the influence of magnetostrictive stresses (emerging in the magnetically inhomogeneous state) on the two-phase domain structure, particularly on the orientation of thelinebreak interphase boundaries.

Phase transition fields as a function of temperature for selected field orientations were determined by observing the domain structure using optical microscopy and the Faraday effect. The experimentally determined phase diagrams were then validated by comparison with theoretical diagrams obtained using the phenomenological model described in the following section.

The first part of the analysis will address changes in the magnetic domain structure near the Morin temperature in relation to the observed magnetic phase transitions, along with a phenomenological model of these transitions for oblique magnetic fields oriented within the ab, ac, and bc planes of the crystal.

4.1. Phenomenological model of the spin reorientation magnetic phase transition in oblique magnetic fields

The theory of spin reorientation phase transitions induced by oblique magnetic fields in magnetic orthorhombic crystals with Dzyaloshinskii–Moriya interaction has been discussed in works [32–36]. An analytical solution describing the spin reorientation magnetic phase transition induced by an oblique field is generally attainable in orthoferrites only for small angles of deviation between the magnetic field and the crystallographic axes. For this

reason, to enable comparison with experimental results obtained over a wide range of field orientations and temperatures, it becomes necessary to employ numerical methods based on a phenomenological model.

The analysis of the spin reorientation transition in dysprosium orthoferrite ($DyFeO_3$) in oblique magnetic fields can be performed using the thermodynamic potential expressed (in spherical coordinates θ and φ for antiferromagnetic vector $\boldsymbol{G}$) as

$$\begin{aligned}\Phi(\theta,\varphi) = &-\tfrac{1}{2}\sum_{i=x,y,z}\left(\chi_{\perp}^{i}+\chi_{\mathrm{R}}^{i}\right)H_i^2 + \tilde{K}_2^{bc}\cos^2(\theta) + \tilde{K}_2^{ab}\sin^2(\theta)\cos^2(\varphi) + K_4^{bc}\cos^4(\theta) + K_4^{ab}\sin^4(\theta)\cos^4(\varphi)\\ &+ K_4\sin^2(2\theta)\cos^2(\varphi) + \frac{\chi^{xy}}{4}H_xH_y\sin^2(\theta)\sin(2\varphi) + \frac{\chi^{xz}}{4}H_xH_z\sin(2\theta)\cos(\varphi) + \frac{\chi^{yz}}{4}H_yH_z\sin(2\theta)\sin(\varphi)\\ &- m_x^0H_x\cos(\theta) - m_z^0H_z\sin(\theta)\cos(\varphi),\end{aligned} \tag{4}$$

where

$$\tilde{K}_2^{bc} = K_2^{bc} - \frac{\chi^{yy}}{2}H_y^2 + \frac{\chi^{zz}}{2}H_z^2, \qquad \tilde{K}_2^{ab} = K_2^{ab} + \frac{\chi^{xx}}{2}H_x^2 - \frac{\chi^{yy}}{2}H_y^2,$$
$$\chi^{ij} = \chi_{\perp}(1+\eta_i)(1+\eta_j), \qquad \text{for } i,j = (x,y,z). \tag{5}$$

The orientations of the magnetic field $\boldsymbol{H}$ should be considered in the crystallographic *ab*, *ac*, and *bc* planes. Among these, the case of an external field applied in the *bc* plane is the simplest to solve and analyze the spin reorientation phase transition in $DyFeO_3$.

4.1.1. Magnetic field $\boldsymbol{H}$ in the crystallographic bc plane

For $\boldsymbol{H} = (0, H_y, H_z)$, the thermodynamic potential takes the form

$$\begin{aligned}\Phi(\theta,\varphi) = &\tilde{K}_2^{bc}\cos^2(\theta) + \tilde{K}_2^{ab}\sin^2(\theta)\cos^2(\varphi)\\ &+ K_4^{bc}\cos^4(\theta) + K_4^{ab}\sin^4(\theta)\cos^4(\varphi)\\ &+ K_4\sin^2(2\theta)\cos^2(\varphi) + \frac{\chi^{yz}}{4}H_yH_z\sin(2\theta)\sin(\varphi)\\ &- m_z^0H_z\sin(\theta)\cos(\varphi).\end{aligned} \tag{6}$$

The equilibrium states in the crystal can be determined by minimizing the thermodynamic potential with respect to the angles θ and φ. The values of these angles in equilibrium are obtained by solving the following system of equations

$$\begin{aligned}\frac{\partial\Phi(\theta,\varphi)}{\partial\theta} = &-\sin(2\theta)\Big[\tilde{K}_2^{bc} - \tilde{K}_2^{ab}\cos^2(\varphi)\\ &+ 2K_4^{bc}\cos^2(\theta) - 2K_4^{ab}\sin^2(\theta)\cos^4(\varphi)\\ &- 4K_4\cos(2\theta)\cos^2(\varphi)\Big] + \frac{\chi^{(yz)}}{2}H_yH_z\cos(2\theta)\\ &\times\sin(\varphi) - m_z^0H_z\cos(\theta)\cos(\varphi) = 0,\end{aligned} \tag{7}$$

$$\begin{aligned}\frac{\partial\Phi(\theta,\varphi)}{\partial\varphi} = &-\sin(2\varphi)\Big[\tilde{K}_2^{ab}\sin^2(\theta) + K_4\sin^2(2\theta)\\ &+ 2K_4^{ab}\sin^4(\theta)\cos^2(\varphi)\Big] + \frac{\chi^{(yz)}}{4}H_yH_z\sin(2\theta)\\ &\times\cos(\varphi) + m_z^0H_z\sin(\theta)\sin(\varphi) = 0,\end{aligned} \tag{8}$$

taking into account the conditions for the minimum of the thermodynamic potential, i.e., $\frac{\partial^2\Phi}{\partial\theta^2} > 0$ and $\frac{\partial^2\Phi}{\partial\theta^2}\frac{\partial^2\Phi}{\partial\varphi^2} - (\frac{\partial^2\Phi}{\partial\theta\partial\varphi})^2 > 0$. Solving the system of equations (7)–(8), after substituting the relevant material constants, leads to the determination of two stable equilibrium states of the type $\Gamma_{1234}(F_xF_yF_zG_xG_yG_z)$, in which both vectors $\boldsymbol{F}$ and $\boldsymbol{G}$ have all three nonzero components. Due to the presence of a term proportional to H_yH_z in the expression for the thermodynamic potential, a solution with $\theta = \pi/2$ does not exist. However, in dysprosium orthoferrite, this term is small, and the deviation of θ from $\pi/2$ in the Γ_{1234} equilibrium states does not exceed 1°. This provides sufficient justification for neglecting the H_yH_z term in the potential expression. Under this approximation, the equilibrium states in an external field $\boldsymbol{H} = (0, H_y, H_z)$ are as follows:

(i) phase $\Gamma_4(F_zG_x)$, for which $\theta = \frac{\pi}{2}$, $\varphi = 0$,

(ii) phase $\Gamma_{14}(F_zG_xG_y)$, for which $\theta = \frac{\pi}{2}$, $\varphi = \varphi_0$.

Near the Morin temperature (T_{M}), for small values of the magnetic field H_z, the angle φ_0 is close to $\pi/2$ — phase $\Gamma_1(G_y)$. The stability regions of phases Γ_{14} and Γ_4 overlap in the phase diagram. Specifically, for temperatures $T < T_{\mathrm{M}}$ and an external magnetic field $\boldsymbol{H} = (0, H_y, H_z)$, a first-order phase transition occurs from state Γ_{14} to state Γ_4. From the condition of equal thermodynamic potentials for these two states, $\Phi(\pi/2, 0) = \Phi(\pi/2, \varphi_0)$, at the phase transition point, the value of the transition field H_p can be determined as

$$H_p(\Gamma_{14}\leftrightarrow\Gamma_4) = \frac{2K_2^{ab}}{m_z^0\cos(\beta)}\,\frac{1-\sqrt{1-\left(1+\frac{K_4^{ab}}{K_2^{ab}}\right)(1-\chi)}}{1-\chi}, \tag{9}$$

where $\chi = 2\chi_{\perp}K_2^{ab}\tan^2(\beta)\,(1+\eta_y)^2/(m_z^0)^2$, and β is the angle between the applied external magnetic field H and the *c* axis of the crystal.

4.1.2. Magnetic field $\boldsymbol{H}$ in the crystallographic ab plane

In the case where the external magnetic field $\boldsymbol{H}$ is oriented within the crystallographic ab plane, the thermodynamic potential (see (4)) can be written in the form

$$\begin{aligned}\Phi(\theta,\varphi) &= \tilde{K}_2^{bc}\cos^2(\theta) + \tilde{K}_2^{ab}\sin^2(\theta)\cos^2(\varphi)\\ &+ K_4^{bc}\cos^4(\theta) + K_4^{ab}\sin^4(\theta)\cos^4(\varphi)\\ &+ K_4\sin^2(2\theta)\cos^2(\varphi) + \frac{\chi^{(xy)}}{4}H_xH_y\sin^2(\theta)\\ &\times\sin(2\varphi) - m_x^0H_x\cos(\theta).\end{aligned} \tag{10}$$

To determine the equilibrium states, the thermodynamic potential is minimized with respect to the variables θ and φ by solving the resulting system of equations

$$\begin{aligned}\frac{\partial\Phi(\theta,\varphi)}{\partial\theta} &= 2\sin(\theta)\cos(\theta)\Big[-\tilde{K}_2^{bc} + \tilde{K}_2^{ab}\cos^2(\varphi)\\ &- 2K_4^{bc}\cos^2(\theta) + 2K_4^{ab}\sin^2(\theta)\cos^4(\varphi)\\ &+ 4K_4\cos(2\theta)\cos^2(\varphi) + \frac{\chi^{(xy)}}{4}H_xH_y\sin(2\varphi)\Big]\\ &+ m_x^0H_x\sin(\theta) = 0,\end{aligned} \tag{11}$$

$$\begin{aligned}\frac{\partial\Phi(\theta,\varphi)}{\partial\varphi} &= -\sin(2\varphi)\sin^2(\theta)\Big[\tilde{K}_2^{ab} + 2K_4^{ab}\sin^2(\theta)\\ &\times\cos^2(\varphi) + 4K_4\cos^2(\theta)\Big]\\ &+ \frac{\chi^{(xy)}}{2}H_xH_y\cos(2\varphi)\sin^2(\theta) = 0.\end{aligned} \tag{12}$$

Taking into account the conditions for the minimum of the potential, it can be shown that in a magnetic field $\boldsymbol{H} = (H_x, H_y, 0)$, two stable phases of the type $\Gamma_{1234}(F_xF_yF_zG_xG_yG_z)$ may exist, with spatial orientation of both vectors $\boldsymbol{F}$ and $\boldsymbol{G}$. At the same time, it should be noted that in this case, a stable $\Gamma_2(F_xG_z)$ phase may also occur, for which $\theta = 0$.

Thus, in dysprosium orthoferrite ($DyFeO_3$) in external magnetic fields $\boldsymbol{H} = (H_x, H_y, 0)$, three magnetic phases may be present:

(i) phase $\Gamma'_{1234}(F_xF_yF_zG_xG_yG_z)$, for which $\theta = \theta_1$, $\varphi = \varphi_1$,
(ii) phase $\Gamma''_{1234}(F_xF_yF_zG_xG_yG_z)$, for which $\theta = \theta_2$, $\varphi = \varphi_2$,
(iii) phase $\Gamma_2(F_xG_y)$, for which $\theta = 0$.

In the case of an external magnetic field applied in the crystallographic ab plane, the spatial orientation of the $\boldsymbol{F}$ and $\boldsymbol{G}$ vectors arises due to the presence of a term proportional to H_xH_y in the expression for the thermodynamic potential. By solving the system of equations, one can determine the values of the angles θ and φ for the equilibrium phases Γ'_{1234} and Γ''_{1234}. The calculated values of these angles lead to the conclusion that, for the spin reorientation process, it is not valid to approximate the rotation of the magnetic vectors $\boldsymbol{F}$ and $\boldsymbol{G}$ as occurring within a single crystallographic plane, as was possible in the case of the field $\boldsymbol{H} = (0, H_y, H_z)$, i.e., in the bc plane.

Near the Morin point, for small magnetic fields $H \ll 2K_2^{bc}/m_x^0$, the angles θ and φ in the phases Γ'_{1234} and Γ''_{1234} can be determined.

For the phase Γ'_{1234}, these angles are

$$\varphi_1 \approx \frac{1}{2}\arcsin\left(\frac{\chi^{(xy)}H_xH_y}{K_4^{ab}}\right), \tag{13}$$

$$\theta_1 \approx \arcsin\left(\frac{m_x^0H_x}{2K_2^{bc}}\right). \tag{14}$$

For the phase Γ''_{1234}, one has $\varphi_2 \approx \frac{\pi}{2} - \varphi_1$ and $\theta_2 \approx \theta_1$. Under these conditions, it is also possible to derive an expression describing the magnetic field of the first-order phase transition between the Γ'_{1234} and Γ''_{1234} phases, i.e.,

$$H_p\left(\Gamma'_{1234} \leftrightarrow \Gamma''_{1234}\right) = \sqrt{\frac{2\left(K_2^{ab}+K_4^{ab}\right)}{\chi_\perp\left[(1+\eta_y)^2\sin^2(\alpha) - (1+\eta_x)^2\cos^2(\alpha)\right]}}. \tag{15}$$

In this relationship, the angle α is defined as the angle between the external magnetic field $\boldsymbol{H}$ and the crystallographic a axis of the $DyFeO_3$ crystal. It is worth noting that the expression appearing in (15) does not include the term $\tilde{K}_2^{ab} + K_4^{ab}$, because this term is approximately equal to zero at the phase transition point.

When an external magnetic field $\boldsymbol{H}$ is applied in the crystallographic ab plane, there is a specific angle $\alpha = \alpha^*$, for which the transition $\Gamma'_{1234} \to \Gamma''_{1234}$ occurs exactly at the Morin temperature $T = T_M$, regardless of the magnitude of the field. In the phase diagram, this is represented by a vertical line. The critical angle α^* can be determined from the following relation

$$\tan(\alpha^*) = \pm\left(\frac{1+\eta_x}{1+\eta_y}\right). \tag{16}$$

4.1.3. Magnetic field $\boldsymbol{H}$ in the crystallographic ac plane

In the case where the external magnetic field $\boldsymbol{H}$ is oriented within the crystallographic ac plane, the thermodynamic potential can be written in the form

$$\begin{aligned}\Phi(\theta,\varphi) &= \tilde{K}_2^{bc}\cos^2(\theta) + \tilde{K}_2^{ab}\sin^2(\theta)\cos^2(\varphi)\\ &+ K_4^{bc}\cos^4(\theta) + K_4^{ab}\sin^4(\theta)\cos^4(\varphi) + K_4\sin^2(2\theta)\\ &\times\cos^2(\varphi) + \frac{\chi^{(xz)}}{4}H_xH_z\sin(2\theta)\cos(\varphi)\\ &- m_x^0H_x\cos(\theta) - m_z^0H_z\sin(\theta)\cos(\varphi).\end{aligned} \tag{17}$$

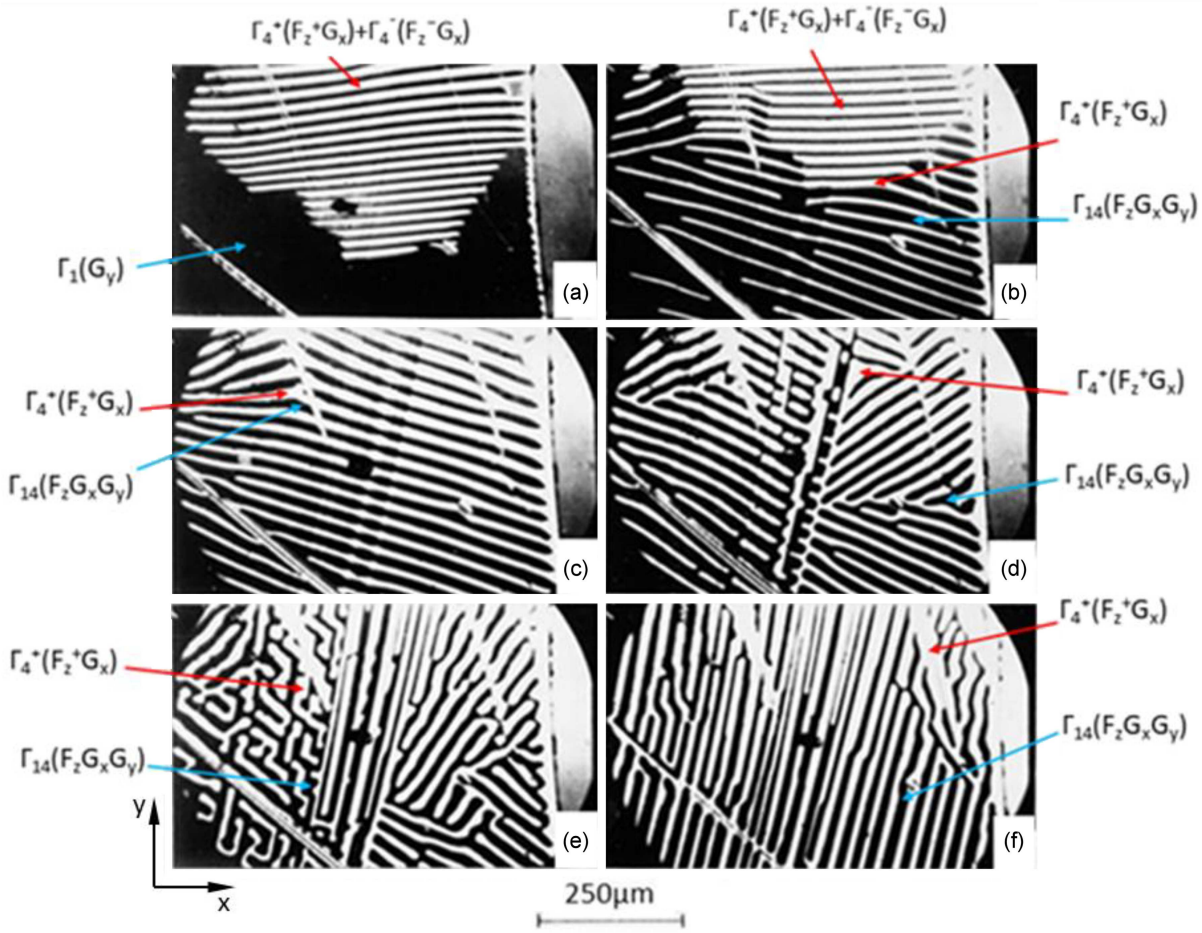

Fig. 10. Magnetic phase domain structure in a $DyFeO_3$ sample (thin plate ~ 40 μm thick, Morin transition temperature $T_M = 51.6$ K; crystallographic c axis perpendicular to the surface; x, y, and z axis orientations corresponding to crystallographic a, b, and c axes, respectively) during the phase transition: (a) $\Gamma_1(G_y) \leftrightarrow \Gamma_4(F_zG_x)$ and (b–f) $\Gamma_{14}(F_zG_xG_y) \leftrightarrow \Gamma_4(F_zG_x)$ in an external magnetic field $\boldsymbol{H} = (0, H_y, H_z)$ at temperature $T = 51$ K; β is the angle of deviation of the magnetic field $\boldsymbol{H}$ from the c axis in the crystallographic bc plane. The values of H [kOe] and β used are: (a) 13.6 and 90° ($\boldsymbol{H} \parallel \boldsymbol{b}$), (b) 12.8 and 89.6°, (c) 11.2 and 89.1°, (d) 8.0 and 88.8°, (e) 6.9 and 88.0°, (f) 0.28 and 0 ($\boldsymbol{H} \parallel \boldsymbol{c}$), respectively.

Following the same approach as in the case of the external magnetic field oriented in the crystallographic ab and bc planes, we find the minimum of the thermodynamic potential with respect to θ and φ, and subsequently determine the angle values for which this minimum occurs, i.e., for which the stable state is realized. The partial derivatives of the potential with respect to these angles form the following system of equations, which must be solved to determine the angles corresponding to the stable magnetic phases

$$\frac{\partial \Phi(\theta,\varphi)}{\partial\theta} = -\sin(2\theta)\Big[\tilde{K}_2^{bc} - \tilde{K}_2^{ab}\cos^2(\varphi) + 2K_4^{bc}\cos^2(\theta) - 2K_4^{ab}\sin^2(\theta)\cos^4(\varphi) - 4K_4 \times \cos(2\theta)\cos^2(\varphi)\Big] + \frac{\chi^{(xz)}}{2}H_xH_z\cos(2\theta)\cos(\varphi) + m_x^0H_x\sin(\theta) - m_z^0H_z\cos(\theta)\cos(\varphi) = 0, \quad (18)$$

$$\frac{\partial(\theta,\varphi)}{\partial\varphi} = -\sin(\varphi)\Big[2\tilde{K}_2^{ab}\sin^2(\theta)\cos(\varphi) + 4K_4^{ab}\sin^4(\theta)\cos^3(\varphi) + 2K_4\sin^2(2\theta)\cos(\varphi) + \frac{\chi^{(xz)}}{4}H_xH_z\sin(2\theta) - m_z^0H_z\sin(\theta)\Big] = 0, \quad (19)$$

while also taking into account the conditions for the minimum of the potential.

One of the solutions to the system of equations (18)–(19) is $\varphi = 0$, $\theta = \theta_1$, which corresponds to the phase $\Gamma_{24}(F_xF_zG_xG_z)$, in which the magnetic vectors $\boldsymbol{F}$ and $\boldsymbol{G}$ are oriented within the crystallographic ac plane. Solving the system of equations (18)–(19) allows us to determine that in the magnetic fields $\boldsymbol{H} = (H_x, 0, H_z)$, two stable magnetic states can exist, namely Γ_{24} and Γ_{1234}.

In dysprosium orthoferrite, these are the magnetic phases observed in external magnetic fields applied in the crystallographic ac plane, i.e., for

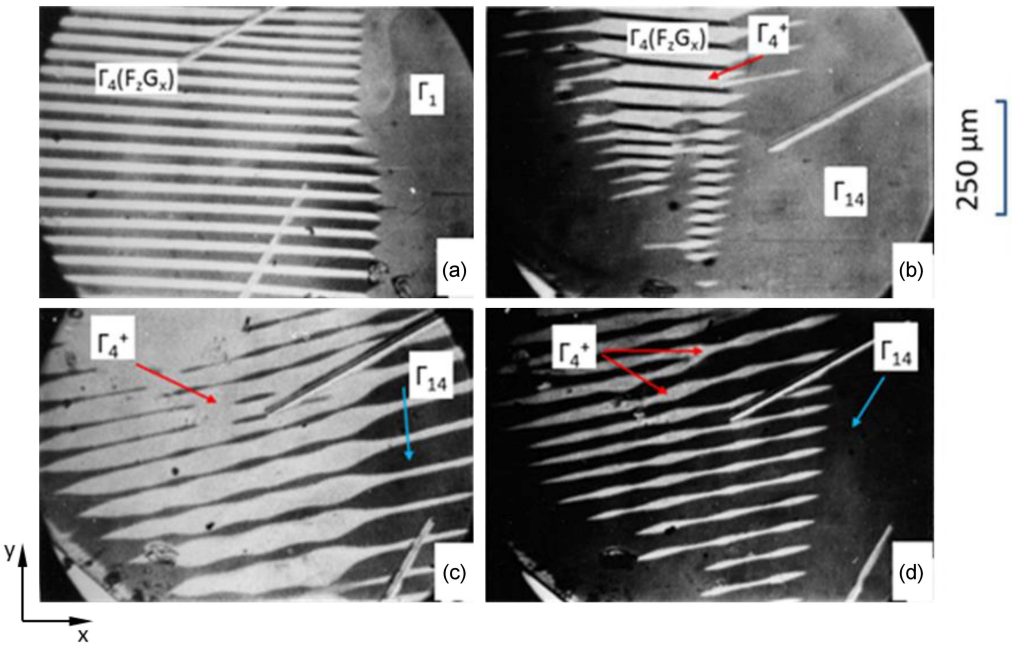

Fig. 11. Magnetic phase domain structure in a $DyFeO_3$ sample (thin plate ~ 40 μm thick; Morin transition temperature $T_M = 51.6$ K; crystallographic c axis perpendicular to the surface; x, y, and z axis orientations correspond to crystallographic a, b, and c axes, respectively) during the $\Gamma_{14}(F_zG_xG_y) \leftrightarrow \Gamma_4(F_zG_x)$ phase transition in an external magnetic field $\boldsymbol{H} = (0, H_y, H_z)$ at $T \approx 7$ K; β is the angle of deviation of the magnetic field $\boldsymbol{H}$ from the c axis in the crystallographic bc plane. The values of H [kOe] and β used are: (a) 6.9 and 90° ($\boldsymbol{H} \parallel \boldsymbol{b}$), (b) 6.7 and 88°, (c) 6.4 and 86°, (d) 6.1 and 84°, respectively.

$\boldsymbol{H} = (H_x, 0, H_z)$. In this configuration, the corresponding angle values θ and φ for the emerging phases are as follows:

(i) $\theta = \theta_1$, $\varphi = 0$ for phase $\Gamma_{24}(F_xF_zG_xG_z)$,

(ii) $\theta = \theta_2$, $\varphi = \varphi_0$ for phase $\Gamma_{1234}(F_xF_yF_zG_xG_yG_z)$.

An external magnetic field $\boldsymbol{H} = (H_x, 0, H_z)$ induces a first-order phase transition in dysprosium orthoferrite ($DyFeO_3$) between the phases Γ_{1234} and Γ_{24}. The case of external fields with this orientation (in the ac plane) is significantly more complex than that of the field orientations in the crystallographic ab and bc planes. For this configuration, it is not possible to derive approximate expressions for determining the angles θ_1, θ_2, and φ_0, or for the transition fields associated with the $\Gamma_{1234} \leftrightarrow \Gamma_{24}$ phase transition.

4.2. Two-phase magnetic domain structures formed during first-order phase transitions in oblique fields

Images of the domain structure observed during phase transitions in a $DyFeO_3$ sample (a plate of 40 μm thickness with the crystallographic c axis perpendicular to the sample surface) in external magnetic fields $\boldsymbol{H}$ oriented in one of the crystallographic ab, ac, or bc planes, are shown in Figs. 10–15. In the case when the external magnetic field lies in the sample plane, i.e., in the ab plane, no periodic (striped) domain structure of interwoven antiferromagnetic and weakly ferromagnetic domains is formed. Instead, a disordered two-phase structure appears, consisting of antiferromagnetic and weakly ferromagnetic phases with two opposite orientations along the c axis. Such structures are shown in Figs. 10a, 11a, 12a–c, and 13a.

Images clearly demonstrate the influence of demagnetizing fields within the weakly ferromagnetic phase, resulting in the formation of a domain structure. The origins of this disordered mixed-phases state (comprising antiferromagnetic and weakly ferromagnetic phases) in a thin $DyFeO_3$ plate with the c axis perpendicular to the surface have been thoroughly discussed in [22, 25, 26], especially the cases involving the presence of external magnetic fields $\boldsymbol{H} \parallel \boldsymbol{a}$ and $\boldsymbol{H} \parallel \boldsymbol{b}$. These studies indicate that such a disordered domain configuration is energetically favorable in the presence of external fields $\boldsymbol{H} = (H_x, H_y, 0)$ during the phase transition $\Gamma'_{1234} \leftrightarrow \Gamma''_{1234}$ (see Fig. 12).

A periodic domain structure representing the coexisting magnetic state of weakly ferromagnetic and antiferromagnetic phases is formed when the external magnetic field is tilted out of the crystal plane, i.e., for $\boldsymbol{H} = (H_x, H_y, H_z)$. This situation is illustrated in Figs. 10b–f, 11c–d, 13c–d, and 14a–b.

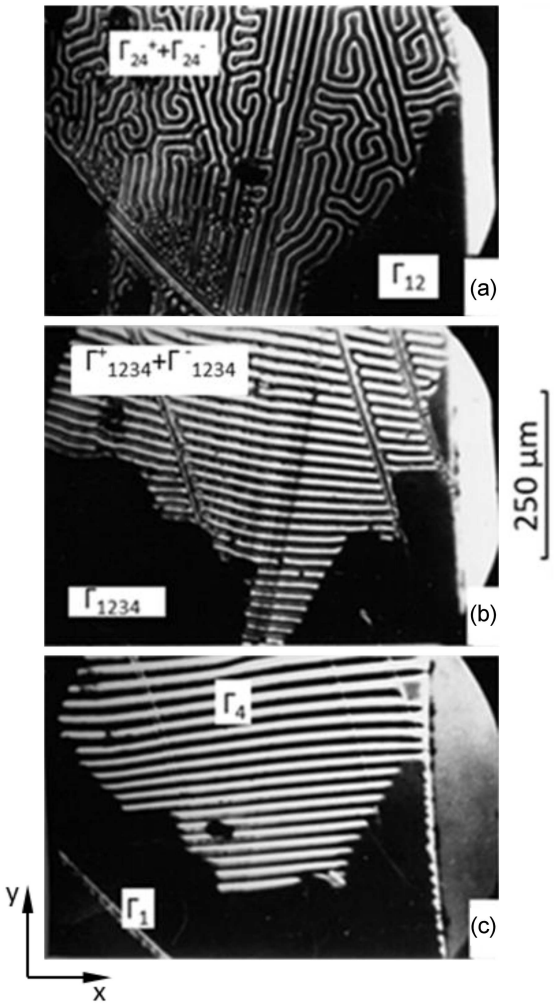

Fig. 12. Magnetic phase domain structure in a $DyFeO_3$ sample (thin plate ~ 40 μm thick, Morin transition temperature $T_M = 51.6$ K; crystallographic c axis perpendicular to the surface; x, y, and z axis orientations correspond to crystallographic a, b, and c axes, respectively) in an external magnetic field $\boldsymbol{H} = (H_x, H_y, 0)$ and for the angle α (between the $\boldsymbol{H}$ direction and the a axis in the sample plane) during the phase transition: (a) $\Gamma_{24}(F_xF_zG_xG_z) \leftrightarrow \Gamma_{12}(F_xG_yG_z)$ for $\boldsymbol{H} \parallel \boldsymbol{a}$ (the coexisting phases are Γ_{12} and Γ_{24} registered at $T \simeq 52.2$ K, $H = 6.3$ kOe, $\alpha = 0^\circ$ ($\boldsymbol{H} \parallel \boldsymbol{a}$)), (b) $\Gamma'_{1234}(F_xF_yF_zG_xG_yG_z) \leftrightarrow \Gamma''_{1234}(F_xF_yF_zG_xG_yG_z)$ in an external magnetic field $\boldsymbol{H} = (H_x, H_y, 0)$ (image taken at $T \simeq 52.2$ K, $H = 8.0$ kOe, $\alpha = 35^\circ$), (c) $\Gamma_1(G_y) \leftrightarrow \Gamma_4(F_zG_x)$ (image taken at $T \simeq 51$ K, $H = 13.6$ kOe, $\alpha = 90^\circ$ ($\boldsymbol{H} \parallel \boldsymbol{b}$)).

The images show the magnetization process in the weakly ferromagnetic state, revealed by the disappearance of one type of domain in this phase.

Figures 10 and 12 present images of the domain structure formed during the phase transition $\Gamma_{14} \leftrightarrow \Gamma_4$, induced by an external magnetic field $\boldsymbol{H} = (0, H_y, H_z)$. In the field $\boldsymbol{H} \parallel \boldsymbol{b}$, as shown in Figs. 10a and 11a, two phases Γ_1 and Γ_4 coexist, with the weakly ferromagnetic phase Γ_4 consisting of domains with orientations $\Gamma_4^+(F_z^+G_x^+)$ and $\Gamma_4^-(F_z^-G_x^-)$. As the external magnetic field is rotated away from the b axis toward the c axis (i.e., out of the sample plane), the domain $\Gamma_4^-(F_z^-G_x^-)$ shrinks and vanishes. A periodic two-phase structure ($\Gamma_1 + \Gamma_4$) is then formed.

There exists a field range $0 < |H_z| < |H_z^s|$, within which two types of coexisting structures are observed, namely antiferromagnetic phase coexisting with a weakly ferromagnetic phase containing only one domain orientation ($\Gamma_1 + \Gamma_4^+$ or $\Gamma_1 + \Gamma_4^-$) and $\Gamma_4^+ + \Gamma_4^-$, depending on the sign of the c-axis component of the external magnetic field. This scenario is depicted in Figs 10b and 11b.

In this context, the field H_z^s refers to the value of the c-axis magnetic field component at which one type of domain in phase Γ_4 disappears, depending on the field's direction.

Observation of the domain walls between the Γ_4^+ and Γ_4^- domains in the Γ_4 phase indicates that these walls lie within the crystallographic ac plane of the sample (Figs. 10a and 11a).

The boundaries separating the weakly ferromagnetic domains from the antiferromagnetic ones lie in a plane perpendicular to the surface of the sample and form an angle with the crystallographic ac plane of the studied sample. Depending on the direction of the external magnetic field $\boldsymbol{H} = (0, H_y, H_z)$, changes in the orientation of these boundaries are observed, as shown in Fig. 10.

The coexistence of magnetic phases $\Gamma'_{1234} \leftrightarrow \Gamma''_{1234}$ during a phase transition induced by a magnetic field $\boldsymbol{H} = (H_x, H_y, 0)$ is illustrated in the domain images in Fig. 12. In the limiting cases, for $\boldsymbol{H} \parallel \boldsymbol{a}$, the coexisting phases are Γ_{12} and Γ_{24}, while for $\boldsymbol{H} \parallel \boldsymbol{b}$, they are Γ_1 and Γ_4. The domain structure images in Fig. 12b were taken in a magnetic field oriented within the sample plane ab, but not aligned with the a or b axes of the crystal. With such a field orientation, a disordered Γ_{1234}-magnetic phase domain structure is observed.

The weakly ferromagnetic phase appears to be inhomogeneous and is divided into domains with opposite ferromagnetic vector directions ($\Gamma_4^+(F_z^+G_x^+)$ and $\Gamma_4^-(F_z^-G_x^-)$) but equal widths. In this case, during the rotation of the external magnetic field $\boldsymbol{H}$ within the crystallographic ab plane, a significant reconstruction of the structure of the weakly ferromagnetic domain structure occurs. This reconstruction begins as a labyrinthine structure for $\boldsymbol{H} \parallel \boldsymbol{a}$ (Fig. 12a), which gradually evolves into a striped structure (Fig. 12a and b) as the angle between $\boldsymbol{H}$ and the a axis increases. During the formation of the striped structure in the weakly ferromagnetic phase, the orientation of the domain walls depends on the orientation (specifically, the direction) of the external magnetic field $\boldsymbol{H}$ within the ab plane.

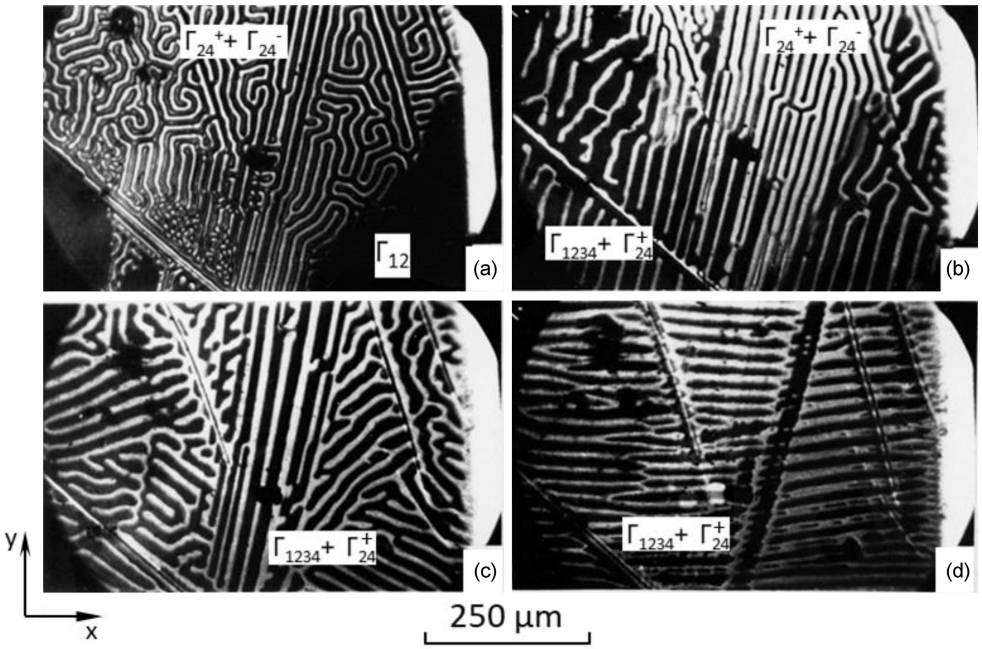

Fig. 13. Magnetic phase domain structure in a $DyFeO_3$ sample (thin plate ~ 40 μm thick; Morin transition temperature $T_M = 51.6$ K; crystallographic c axis perpendicular to the surface; x, y, and z axis orientations correspond to crystallographic a, b, and c axes, respectively) during the $\Gamma_{1234} \leftrightarrow \Gamma_{24}$ phase transition in an external magnetic field $\boldsymbol{H} = (H_x, 0, H_z)$ at $T \approx 52.2$ K; γ is the angle between $\boldsymbol{H}$ direction and the c axis in the crystallographic ac plane of the sample. The values of H [kOe] and γ used are: (a) 6.3 and 90° ($\boldsymbol{H} \parallel \boldsymbol{a}$), (b) 6.7 and 89°, (c) 9.6 and 88.6°, (d) 16.0 and 88.3°, respectively.

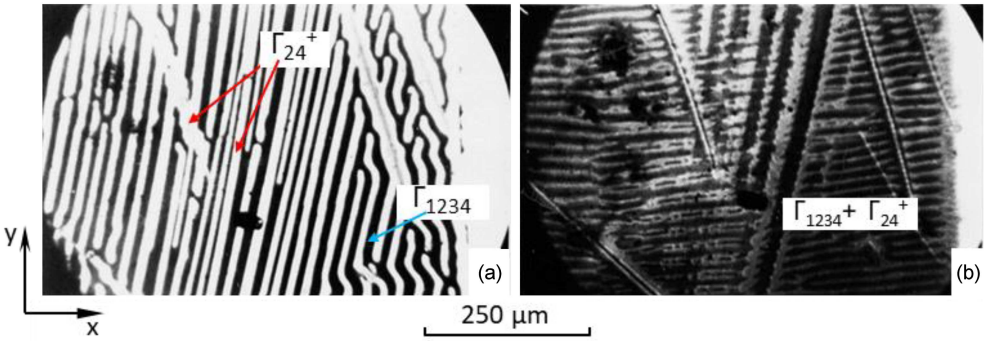

Fig. 14. Magnetic phase domain structure in a $DyFeO_3$ sample (thin plate ~ 40 μm thick; Morin transition temperature $T_M = 51.6$ K; crystallographic c axis perpendicular to the surface; x, y, and z axis orientations correspond to crystallographic a, b, and c axes, respectively) during the $\Gamma_{1234} \leftrightarrow \Gamma_{24}$ phase transition in an external magnetic field $\boldsymbol{H} = (H_x, 0, H_z)$ at $T \approx 47$ K; γ is the angle between the $\boldsymbol{H}$ direction and the c axis in the crystallographic ac plane of the sample. The values of H [kOe] and γ used are: (a) 0.32 and 45°, (b) 16 and 88°, respectively.

However, in the crystallographic ac plane under the condition $\boldsymbol{H} \parallel \boldsymbol{b}$ (see Fig. 12c), the weakly ferromagnetic domain structure is perpendicular to the sample surface. As the field is tilted away from the b axis (see Fig. 12b), the structure becomes inclined accordingly.

Figures 13 and 14 show domain structure images of phase domains composed of two phases formed during a magnetic phase transition $\Gamma_{24} \leftrightarrow \Gamma_{1234}$, induced by a field $\boldsymbol{H} = (H_x, 0, H_z)$, i.e., in the crystallographic ac plane. During such a transition, in a sample with the c axis perpendicular to its surface, a periodic two-phase domain structure emerges, consisting of antiferromagnetic and weakly ferromagnetic domains. An exception occurs when the field orientation is close to the a axis. For magnetic fields with the value $\boldsymbol{H}_z$ in the range $0 < H_z < H_z^s$, the sample may simultaneously contain regions with two different types of domain structures — $\Gamma_{1234} + \Gamma_{24}^+$ and $\Gamma_{24}^+ + \Gamma_{24}^-$. This situation is illustrated in Fig. 13b.

As the field increases, the two-phase domain structure becomes more complex (see Figs. 13d and 14b). Boundaries appear between phases with new orientations, which are no longer perpendicular to the sample surface. Simultaneously, there is a tendency for the boundaries to align along directions close to the crystallographic axis a.

The occurrence of two-phase striped domain structures is limited to a certain range of magnetic fields that can be associated with the demagnetizing fields. The formation and disappearance of such a state can be generally expressed as [37]

$$H_1 = H_p + 4\pi\hat{N}\, m_{\text{afm}},$$
$$H_2 = H_p + 4\pi\hat{N}\, m_{\text{wfm}}, \tag{20}$$

where $\hat{N}$ is the demagnetization factor tensor, m_{afm} and m_{wfm} are the magnetic moments in the antiferromagnetic phase and in the weak ferromagnetic phase, respectively.

In oblique magnetic fields, due to the differing orientations of $\boldsymbol{m}$ and $\boldsymbol{H}$, the internal field H_{int} is given by $H_{int} = H - 4\pi\hat{N}\langle m\rangle$. This internal field therefore changes not only due to the variation of coexisting phases, but also due to the changing direction of $\boldsymbol{H}$. As a result, in a $DyFeO_3$ sample, the value of the transition field varies depending on the orientation of the external magnetic field $\boldsymbol{H}$ relative to the crystallographic axes. Thus, the transition fields H_p in the expressions for H_1 and H_2 are different.

Consequently, the field range in which the observed phases coexist also depends on ΔH_p, and it can be expressed by the following formula

$$\Delta H = 4\pi\hat{N}\,(m_{\text{wfm}} - m_{\text{afm}}) + \Delta H_p. \tag{21}$$

In studies in oblique magnetic fields conducted on dysprosium orthoferrite ($DyFeO_3$) with the crystallographic axis c perpendicular to the sample surface, the ΔH field range corresponding to the coexistence of phases did not exceed 300 Oe.

In the case of the formation of a two-phase AFM + WFM (antiferromagnetic + weakly ferromagnetic) structure with $\boldsymbol{H}$ oriented in the crystallographic ab plane, the width of the coexistence range (both in terms of magnetic field and temperature) depends more strongly on the sample inhomogeneity than on the demagnetizing fields.

4.3. The influence of magnetostriction on the two-phase domain structure

Detailed analysis of the two-phase domain structure images in disprosium orthoferrite ($DyFeO_3$) — in a sample with the crystallographic c axis perpendicular to its surface and subjected to an oblique external magnetic field $\boldsymbol{H} = (0, H_y, H_z)$ — reveals clear patterns in the orientation of interphase boundaries. These boundaries exhibit orientation changes that depend on the direction of the applied magnetic field (Fig. 10). Careful examination of such two-phase structures in this sample and magnetic field configuration allows one to determine the relationship between the orientation of the interphase boundaries and the directions and polarities of the ferromagnetic and antiferromagnetic vectors in the coexisting phases.

Similar regularities in the orientation of phase (magnetic) boundaries have been observed in two-phase domain structures in oblique magnetic fields $\boldsymbol{H} = (H_x, 0, H_z)$, although in this configuration the patterns appear to be less sharply defined.

The observed regularities in boundary orientation for both of these external field configurations (with respect to the crystallographic axes of the sample) can be interpreted within a framework that considers the influence of magnetostrictive stress on boundary orientation. It is known that in magnetic materials subdivided into domains with non-180° walls, elastic stresses can arise [38, 39]. These stresses originate from differing magnetostrictive deformations across the magnetic phases. Such stresses may influence the orientation of the phase boundaries [40–42].

In $DyFeO_3$, during a spin reorientation transition induced by a magnetic field, the phase boundaries between the antiferromagnetic and weakly ferromagnetic regions are not 180° walls. Moreover, the field-induced phase transition is of the first order, which in antiferromagnets typically involves a significant jump in magnetostrictive deformation. It is therefore reasonable to assume that magnetoelastic interactions play a significant role in forming the equilibrium two-phase domain structure.

Additionally, it can be concluded that the effect of magnetostriction on the domain structure in a crystal depends on the ratio of the magnetoelastic energy to the energy of demagnetizing field. In magnetic materials with multiple sublattices, the influence of magnetoelastic interactions on domain formation can be especially pronounced. This results from the fact that the sublattice magnetic moment (used to describe magnetostrictive energy) is usually much larger than the net magnetic moment, which determines the energy of demagnetizing fields [43].

Unlike the influence of magnetostrictive stress in uniaxial ferromagnets discussed in [40–42], in antiferromagnets under the influence of an external magnetic field, the orientation of domain walls may be dominantly affected by magnetostriction, which is linearly dependent on the magnetic field strength. In $DyFeO_3$, in the magnetic field region of the phase transition $\Gamma_{14} \leftrightarrow \Gamma_4$, the contribution of linear magnetostriction is comparable to that of quadratic magnetostriction [44]. Linear magnetostriction may lead to a dependence of the interphase boundary orientation on the directions of the $\boldsymbol{F}$ and $\boldsymbol{G}$ vectors in the coexisting phases.

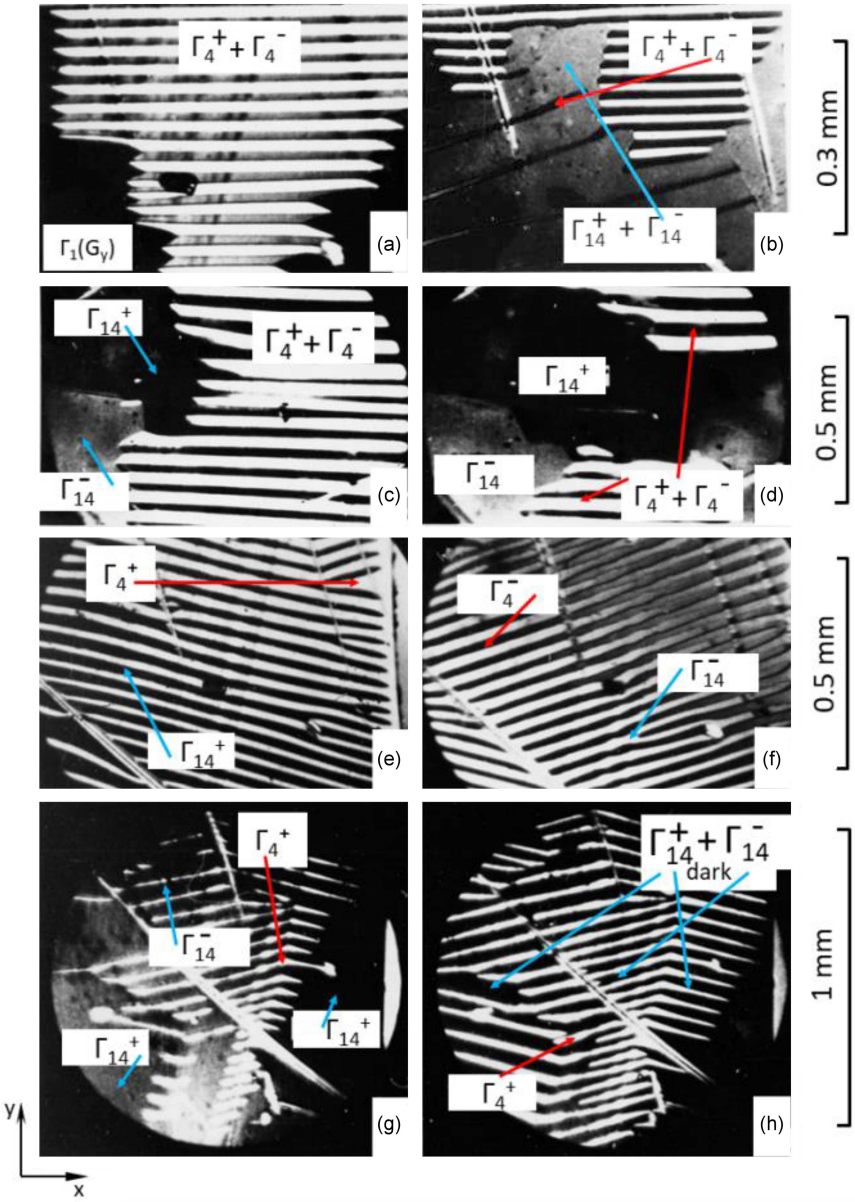

Fig. 15. Magnetic phase domain structure in $DyFeO_3$ (thin plate $\approx 40\ \mu$m thick, Morin transition temperature $T_M = 51.6$ K, crystallographic c axis perpendicular to the surface; x, y, and z axis orientations correspond to crystallographic a, b, and c axes, respectively) during the $\Gamma_4(F_zG_x) \leftrightarrow \Gamma_{14}(F_zG_xG_y)$ phase transition in an external magnetic field $\boldsymbol{H} = (0, H_y, H_z)$; β is the angle between $\boldsymbol{H}$ and the c axis in the crystallographic bc plane of the sample. When $H_z < H_z^s$, the T [K], H_y [kOe], H_z [Oe], γ values are, respectively: (a) 16, 11.6, 0, 90° ($\boldsymbol{H} \parallel \boldsymbol{b}$), (b) 51, 12.8, 50, 89.8°, (c, d) 8, 7.6, $\simeq$ 110, $\simeq$ 89.2°. Images (c, d) were registered at the same conditions, but with different magnetic history. When $H_z > H_z^s$, the T [K], H_y [kOe], H_z [Oe], γ values are: (e) 50, 16, 260, 89°, (f) 50, 16, −260, 91°, (g, h) 18, 12.5, 200, 89.1°. Images (g, h) were registered at the same conditions, but with different magnetic history.

4.4. Dependence of the interphase boundary orientation on the orientation of the $\boldsymbol{F}$ and $\boldsymbol{G}$ vectors in coexisting phases during the transition $\Gamma_{14} \leftrightarrow \Gamma_4$ in the field $\boldsymbol{H} = (0, H_y, H_z)$

Identifying regularities in the orientation of the interphase boundaries during a magnetic phase transition involving coexisting phases requires an analysis of domain structures formed in an external magnetic field. Such two-phase domain structures are presented in Fig. 15a. The image in Fig. 15a shows the domain structure in the magnetic field $\boldsymbol{H} \parallel \boldsymbol{b}$, while the images in Fig. 15b–d show structures in the field $\boldsymbol{H} = (0, H_y, H_z)$, when $H_z < H_z^s$.

In Fig. 15, one can see a "sawtooth" configuration of the boundaries separating the antiferromagnetic phase from the weakly ferromagnetic phase

(subdivided into domains). The interphase boundary lies perpendicular to the sample surface and is tilted at an angle ψ relative to the crystallographic ac plane of the sample. This tilt depends on the specific types of neighboring magnetic phases. When the phase $\Gamma_{14}^{+}(F_z^{+}, G_x^{+}, G_y^{+})$ in oblique fields or the phase $\Gamma_1^{+}(G_y^{+})$ in the field $\boldsymbol{H} \parallel \boldsymbol{b}$ coexists with the phase $\Gamma_4^{+}(F_z^{+}G_x^{+})$, the interphase boundaries are oriented at $+\psi$ relative to the ac plane. However, the boundaries between the phases $\Gamma_{14}^{+}(F_z^{+}G_x^{+}G_y^{+})$ and $\Gamma_4^{-}(F_z^{-}G_x^{-})$ are oriented at $-\psi$ relative to the ac plane.

The observed variations in the orientation of the interphase boundaries with respect to the ac plane reflect the dependence of their direction on the orientation of the $\boldsymbol{F}$ (ferromagnetic) and $\boldsymbol{G}$ (antiferromagnetic) vectors in the weakly ferromagnetic phase $\Gamma_4(F_zG_x)$. Reversing the orientation of $\boldsymbol{F}$ and $\boldsymbol{G}$ leads to a change in the angle ψ to its negative counterpart with respect to the crystallographic ac plane.

Furthermore, the interphase boundary orientation also depends on the direction of the $\boldsymbol{G}$ vector in the antiferromagnetic phase. This is evident in Fig. 15c and d, where the antiferromagnetic domains $\Gamma_{14}^{+}(F_z^{+}G_x^{+}G_y^{+})$ and $\Gamma_{14}^{-}(F_z^{+}G_x^{+}G_y^{-})$ coexist in the sample. These results clearly show that the boundaries between $\Gamma_{14}^{+}(F_z^{+}G_x^{+}G_y^{+})$ and $\Gamma_4^{+}(F_z^{+}G_x^{+})$, as well as $\Gamma_{14}^{-}(F_z^{+}G_x^{+}G_y^{-})$ and $\Gamma_4^{-}(F_z^{-}G_x^{-})$, are inclined at $+\psi$, while the boundaries between $\Gamma_{14}^{-}(F_z^{+}G_x^{+}G_y^{-})$ and $\Gamma_4^{+}(F_z^{+}G_x^{+})$ and between $\Gamma_{14}^{+}(F_z^{+}G_x^{+}G_y^{+})$ and $\Gamma_4^{-}(F_z^{-}G_x^{-})$ are inclined at $-\psi$ relative to the ac plane.

Although it is difficult to determine the angle ψ precisely based solely on Fig. 15, measurements indicate that the boundary tilt from the ac plane is approximately symmetric in both directions. In Fig. 15a, the angle ψ is between 30° and 40°, and in Fig. 15b–d it is between 40° and 50°. Notably, in Fig. 15b the magnetic boundary between weakly ferromagnetic domains of phase $\Gamma_4^{+}(F_z^{+}G_x^{+})$ under the same external conditions (field and temperature) forms an angle of $\approx 20°$ with the ac plane.

In the case of a striped two-phase domain structure (antiferromagnetic + weakly ferromagnetic) formed in an external magnetic field $\boldsymbol{H} = (0, H_y, H_z)$ with a nonzero component $H_z \geq H_z^s$ (see Fig. 15e and h), the same regularities in the phase boundary orientation apply as in the previously described scenario. Figure 15e and f clearly shows a change in the interphase boundary orientation depending on the direction of the $\boldsymbol{F}$ and $\boldsymbol{G}$ vectors in the weakly ferromagnetic domains. Conversely, Fig. 15g and h illustrates how the interphase boundary orientation changes depending on the direction of the $\boldsymbol{G}$ vector in the antiferromagnetic domains.

The images in Fig. 15e and f were taken in external magnetic fields of opposite polarity, i.e., $H_z > 0$ in panel e and $H_z < 0$ in panel f. In the first case, the two-phase structure consists of the domains $\Gamma_{14}^{+}(F_z^{+}G_x^{+}G_y^{+})$ and $\Gamma_4^{+}(F_z^{+}G_x^{+})$, while in the second it consists of $\Gamma_{14}^{+}(F_z^{-}G_x^{-}G_y^{+})$ and $\Gamma_4^{-}(F_z^{-}G_x^{-})$. The direction of the interphase boundary inclination relative to the ac plane is opposite for these two field configurations.

The images in Fig. 15g and h show that in certain sample regions, $\Gamma_{14}^{+}(F_z^{+}G_x^{+}G_y^{+})$ coexists with $\Gamma_4^{+}(F_z^{+}G_x^{+})$, and in others, $\Gamma_{14}^{-}(F_z^{+}G_x^{+}G_y^{-})$ with $\Gamma_4^{+}(F_z^{+}G_x^{+})$. These images clearly demonstrate the difference in the boundary inclination depending on whether the coexisting antiferromagnetic phase is $\Gamma_{14}^{+}(F_z^{+}G_x^{+}G_y^{+})$ or $\Gamma_{14}^{-}(F_z^{+}G_x^{+}G_y^{-})$. The observed tilt angle ψ in the striped two-phase structure ranges between 13° and 19° in either direction from the ac plane.

Reducing the H_y component of the external magnetic field results in a change in the interphase boundary orientation (Fig. 10). During this transformation, elastic stresses associated with crystal inhomogeneities play a significant role (Fig. 10a).

However, in an external magnetic field $\boldsymbol{H} \parallel \boldsymbol{c}$, the orientation of the interphase boundaries is not dependent on differences in the orientation of the $\boldsymbol{F}$ and $\boldsymbol{G}$ vectors in the coexisting phases (Fig. 10f).

4.5. Magnetic phase diagrams for $DyFeO_3$ in oblique magnetic fields

Detailed analysis of archived photographic images of two-phase domain structures has made it possible to determine the values of the magnetic field and temperature at which first-order phase transitions occur for various specified orientations of the external magnetic field $\boldsymbol{H}$. Based on this analysis, magnetic phase diagrams were constructed for the investigated dysprosium orthoferrite $DyFeO_3$ across a wide temperature range and for many magnetic field orientations. This enables a comprehensive examination of the evolution of these diagrams as the magnetic field orientation changes within selected crystallographic planes of the sample.

Experimental phase diagrams obtained for $DyFeO_3$, depending on the external magnetic field $\boldsymbol{H}$ oriented in the crystallographic planes ab, ac, and bc, can be compared with diagrams obtained from numerical calculations based on the analysis of phenomenological model presented in the first part of this chapter. Almost all of the constants required to calculate the thermodynamic potential (4) for $DyFeO_3$ were determined through magneto–optical studies and direct visualization (photographs of the structure during phase transitions) of spin-reorientation transitions, as well as from phase diagrams for external magnetic fields aligned with the orthorhombic axes of the crystal. The results of calculations of the equilibrium magnetic parameters of the phases and their

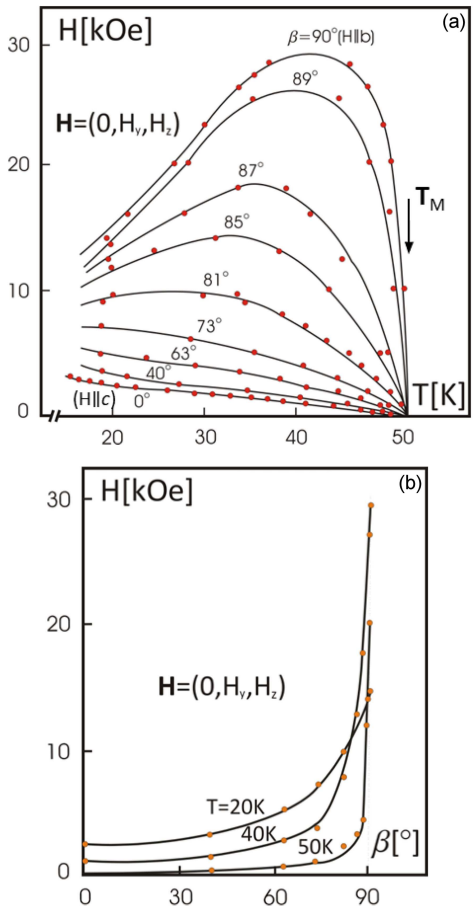

Fig. 16. The $\Gamma_{14}(F_zG_xG_y) \leftrightarrow \Gamma_4(F_zG_x)$ phase transition field, H_p, plotted as a function of (a) temperature T and (b) β, i.e., the angle between the $\boldsymbol{H}$ direction and the crystallographic c axis in the crystallographic bc plane of the sample; $\boldsymbol{H} = (0, H_y, H_z)$. Measurements were performed for dysprosium orthoferrite sample (a plate perpendicular to the crystallographic c axis). On the H–T diagram, the β angles are indicated along the curves. On the H–β diagram, the T values are indicated along the curves.

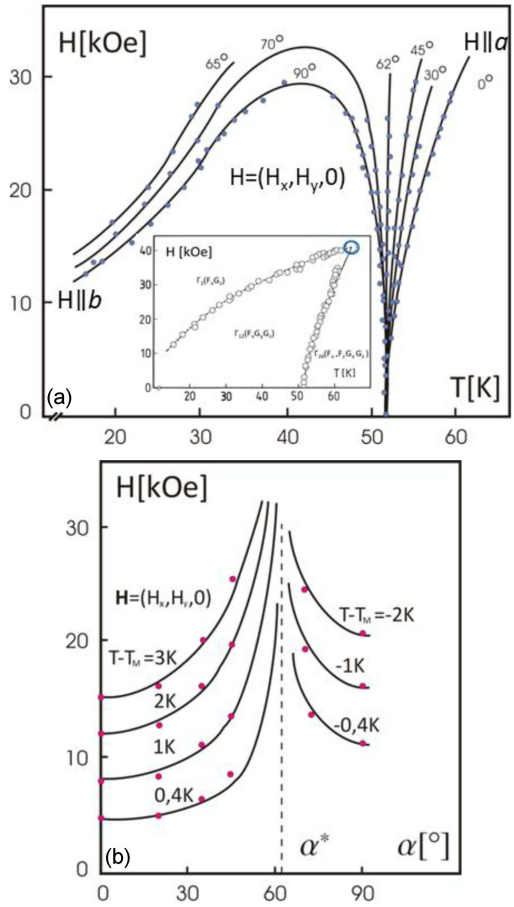

Fig. 17. Phase diagrams in the (a) H–T and (b) H–α plane for $DyFeO_3$ in an external magnetic field $\boldsymbol{H} = (H_x, H_y, 0)$; α is the angle between the direction of $\boldsymbol{H}$ and the crystallographic a axis in the crystallographic ab plane of the sample. On the H–T diagram, the α angles are indicated along the curves. On the H–α diagram, the T values are indicated along the curves. The inset present the phase transition diagram (based on [26]) for $\alpha = 0$.

dependence on the external magnetic field are also presented, which allow for a much more complete picture of spin-reorientation phase transitions in $DyFeO_3$ in oblique magnetic fields.

4.5.1. Magnetic phase diagrams obtained experimentally in the H–T and H–angle planes for magnetic fields oriented in the crystallographic ab, ac, and bc planes of the studied samples

The magnetic phase diagrams in the H–T and H–angle (α, β, γ) planes for $DyFeO_3$, obtained experimentally in external magnetic fields oriented in the crystallographic planes ab, ac, and bc, are presented in Figs. 16, 17, and 18, respectively.

If the formation of a periodic structure was observed in the sample during the phase transition process, then the experimental determination of the transition field was based on identifying the field at which the striped domain structure of coexisting phases nucleated within the homogeneous antiferromagnetic phase. Neglecting the small magnetic moment of the antiferromagnetic phase, and in accordance with (20), it can be assumed that the external magnetic field corresponds to the phase transition field $H_p \approx H_1$.

If, during the phase transition in $\boldsymbol{H}$ within the crystallographic ab plane, irregular regions with different magnetic orderings coexisted, the transition field and transition temperature were defined as the average values of those quantities at which coexistence of magnetic phases was observed. Such observations were carried out over a representative sample area with a diameter of ≈ 0.1 mm. The range of

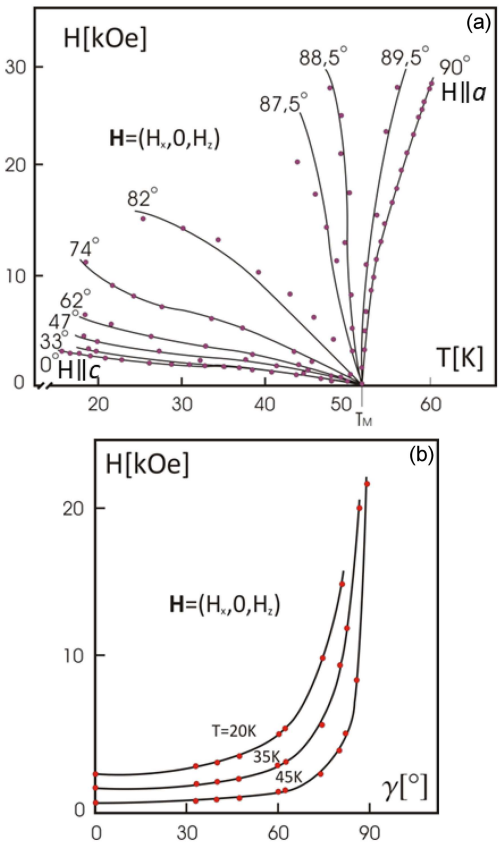

Fig. 18. Phase diagrams in the (a) H–T and (b) H–γ plane for $DyFeO_3$ in an external magnetic field $\boldsymbol{H} = (H_x, 0, H_z)$; γ is the angle between the direction of $\boldsymbol{H}$ and the crystallographic c axis in the crystallographic ac plane of the sample. In the H–T diagram, the γ values are indicated along the curves. In the H–γ diagram, the T values are shown along the curves.

magnetic fields, in which the weakly ferromagnetic and antiferromagnetic phases (for a given temperature) coexist, did not exceed 300 Oe. Similarly, the range of coexistence for temperature across different magnetic fields did not exceed 0.2 K for all field orientations within the ab plane.

As with fields oriented along the orthorhombic crystal axis, practically no hysteresis phenomena were observed in the case of oblique fields. The maximum thermal hysteresis observed during heating and cooling in a constant magnetic field was 0.1–0.2 K. Therefore, it can be concluded that hysteresis phenomena did not affect the experimentally obtained phase diagrams presented in the figures.

Figure 16a and b shows the H–T and H–β phase diagrams, respectively, for $DyFeO_3$ in the external magnetic field $\boldsymbol{H}$ oriented in the crystallographic plane bc. The lines on these diagrams represent first-order phase transitions and separate the regions of the antiferromagnetic phase Γ_{14} (when $H < H_p$) and the weakly ferromagnetic phase Γ_4 (when $H > H_p$). For $\boldsymbol{H} \parallel \boldsymbol{b}$, the transition line separates the Γ_1 and Γ_4 phases. These diagrams clearly show a strong dependence of the transition field H_p on the orientation angle β of the external field $\boldsymbol{H}$ near $\beta \approx 90°$, especially at temperatures close to the Morin temperature T_M. For angles $0° < \beta < 70°$, the observed change in H_p is minimal.

Figure 17a and b shows the H–T and H–α phase diagrams, respectively, for $DyFeO_3$ in the external magnetic field $\boldsymbol{H}$ oriented in the crystallographic ab plane. In this case, first-order phase transition lines separate regions of different phases Γ'_{1234} and Γ''_{1234}. For $\boldsymbol{H} \parallel \boldsymbol{a}$, these are phases Γ_{24} and Γ_{12}; for $\boldsymbol{H} \parallel \boldsymbol{b}$, phases Γ_4 and Γ_1. A special feature of this field orientation is the angle $\alpha = \alpha^*$, at which, at $T = T_M$, the phases Γ'_{1234} and Γ''_{1234} are energetically equivalent over the entire investigated magnetic field range $0 < H < 30$ kOe. The phase transition from the antiferromagnetic Γ''_{1234} to the weakly ferromagnetic Γ'_{1234} is observed at $T < T_M$ only for angles α in the range $\alpha^* < \alpha < 90°$. Conversely, the transition from the weakly ferromagnetic Γ'_{1234} to the antiferromagnetic Γ''_{1234} occurs at $T > T_M$ only for $0° < \alpha < \alpha^*$.

Figure 18a and b shows the H–T and H–γ phase diagrams, respectively, for $DyFeO_3$ in the external magnetic field $\boldsymbol{H}$ in the crystallographic ac plane. First-order phase transition lines separate the antiferromagnetic Γ_{1234} and the weakly ferromagnetic phases Γ_{24}. For $\boldsymbol{H} \parallel \boldsymbol{a}$, the phases are Γ_{12} and Γ_{24}; for $\boldsymbol{H} \parallel \boldsymbol{c}$, the phases are Γ_{14} and Γ_4. At $T > T_M$, in a narrow range of angles γ such that $\gamma^* < \gamma < 90°$ ($\gamma^* \approx 89°$), the transition $\Gamma_{24} \leftrightarrow \Gamma_{1234}$ is observed. At $T < T_M$, the reverse transition $\Gamma_{1234} \leftrightarrow \Gamma_{24}$ occurs for $0° < \gamma < \gamma^*$. A strong dependence of the transition field H_p on the orientation of the external field in the bc plane is thus observed for γ close to 90°, whereas near the c axis the value of H_p changes very little with variations in γ.

4.5.2. Determination of the temperature dependence of magnetic constants in $DyFeO_3$

To perform the calculations necessary to construct magnetic phase diagrams in the H–T plane and the H-field orientation angle plane, it is essential to determine how the magnetic constants vary with temperature.

Specifically, to determine the second-order magnetic anisotropy constant K_2^{ab} for temperatures $T < T_M$, one should use experimental data from the observations of the domain structure during spin reorientation in an external magnetic field oriented along the crystallographic c axis ($\boldsymbol{H} \parallel \boldsymbol{c}$). Under these conditions, the anisotropy constant can be expressed by

$$K_2^{ab} = \frac{m_z^0 \, H_p(\Gamma_{14} \leftrightarrow \Gamma_4)}{2\cos(\varphi_p)}, \tag{22}$$

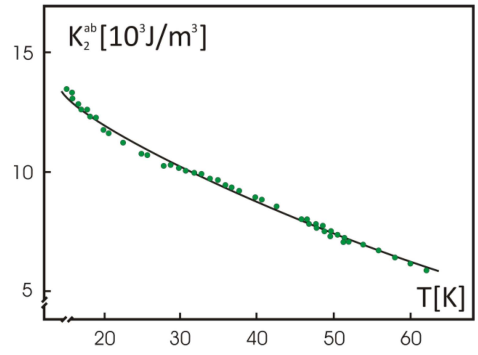

Fig. 19. Temperature dependence of the second-order magnetic anisotropy constant K_2^{ab} in $DyFeO_3$.

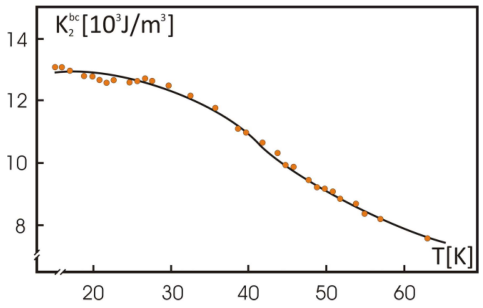

Fig. 20. Temperature dependence of the second-order anisotropy constant K_2^{bc} in $DyFeO_3$.

where $H_p(\Gamma_{14} \leftrightarrow \Gamma_4)$ and φ_p denote, respectively, the phase transition field and the threshold deflection angle of the antiferromagnetic vector $\boldsymbol{G}$ for the orientation of the external magnetic field $\boldsymbol{H}$ along the crystallographic axis c. If the dependencies $H_p(T)$ and $\varphi_p(T)$, as well as $m_z^0(T)$, are known, then using the presented formula (22), one obtains the temperature dependence of the second-order anisotropy constant $K_2^{ab}(T)$. The calculation results are presented in Fig. 19. The determined dependence $K_2^{ab}(T)$ allows for the calculation of the fourth-order anisotropy constant $K_4^{ab}(T)$ for temperatures $T < T_{\mathrm{M}}$, because they are related by the expression

$$K_4^{ab} = -K_2^{ab}\left(1 - \frac{m_z^0\, H_p(\Gamma_{14} \leftrightarrow \Gamma_4)}{2K_2^{ab}}\right)^2. \tag{23}$$

The constant calculated on this basis is practically independent of temperature and amounts to $K_4^{ab} = -7.2 \times 10^4$ erg/cm^3.

The determined dependence $K_2^{ab}(T)$ for temperatures within the range $T_{\mathrm{M}} < T < T_{cr}$ has the form

$$K_2^{ab} = -K_4^{ab} - \frac{1}{2}H_p^2(\Gamma_{12} \leftrightarrow \Gamma_{24})\left[\chi_\perp (1+\eta_x)^2 + \frac{4K_4 - K_4^{ab}}{H_p^2(\Gamma_{12} \leftrightarrow \Gamma_2)}\right] \tag{24}$$

and makes it possible to use the experimentally determined temperature dependences of the transition fields $H_p(\Gamma_{12} \leftrightarrow \Gamma_{24})$ and $H_p(\Gamma_{12} \leftrightarrow \Gamma_2)$, obtained under the conditions $\boldsymbol{H} \parallel \boldsymbol{a}$ and presented in [26], as well as the dependences $\eta_x(T)$ and $K_4(T)$, which will be presented later in this work. The value $\chi_\perp = 6 \times 10^{-5}$ is taken from [45]. The results of the calculations are shown in Fig. 19 with a solid line.

The dependence $K_2^{ab}(T)$ is theoretically described by two temperature-dependent terms that alter the ground state. These are: a term that contributes through quantum-mechanical excitations (so-called van Vleck contributions [3, 46]) and a second term that is proportional to T^{-1}. The resulting dependence $K_2^{ab}(T)$ then takes the form

$$K_2^{ab}(T) = K_{20}^{ab} + K_{\mathrm{VF}}^{ab} \tanh\left(\frac{E_1}{2k_{\mathrm{B}}T}\right) + \frac{\chi}{T}, \tag{25}$$

where k_{B} is the Boltzmann constant. Very good agreement with the dependence obtained from experimental data is achieved for the following constants: $K_{20}^{ab} = -0.25 \times 10^4$ erg/cm^3, $K_{\mathrm{VF}}^{ab} = 1.08 \times 10^5$ erg/cm^3, $\chi = 4.4 \times 10^4$ erg K/cm^3, $E_1 = 52.5$ cm^{-1} taken from [47]. The results obtained from the calculations are shown by a solid line in Fig. 19.

It should be noted that the temperature dependence of the magnetic moment is described by the relation

$$m_z^0(T) = m_0 + m_{\mathrm{VF}} \tanh\left(\frac{E_1}{2k_{\mathrm{B}}T}\right) + \frac{c}{T}. \tag{26}$$

The values of the constants in this relation are as follows: $m_0 = 11$ emu/cm^3, $m_{\mathrm{VF}} = 3$ emu/cm^3, $c = 130$ emu K/cm^3. In fact, (26) describes $m_z^0(T)$ very well in dysprosium orthoferrite.

The temperature dependence of the second-order anisotropy constant $K_2^{bc}(T)$ can be calculated using the formula

$$K_2^{bc} + K_4^{bc} = \frac{1}{2}m_x^0\, H_p(\Gamma_{12} \leftrightarrow \Gamma_2), \tag{27}$$

which is obtained from relation (11) by assuming $\varphi = \frac{\pi}{2}$ and $\theta = 0$. To calculate $K_2^{bc}(T)$, the experimentally determined dependence of the second-order phase transition field between the $\Gamma_{12} \leftrightarrow \Gamma_2$ phases (determined for $\boldsymbol{H} \parallel \boldsymbol{a}$) is also used, as well as data from magnetic measurement of $m_x^0(T)$. When performing calculations for $DyFeO_3$, one should adopt the approximation $K_2^{bc} \gg K_4^{bc}$, which is very well satisfied in the case of this material, since K_2^{bc} exceeds the fourth-order anisotropy constants K_4^{bc} and K_4 by an order of magnitude. The resulting dependence $K_2^{bc}(T)$ is shown in Fig. 18.

Based on the experimentally obtained dependence of the phase transition field $H_{p(\Gamma_1 \leftrightarrow \Gamma_4)}(T)$ as a function of temperature T for the case $\boldsymbol{H} \parallel \boldsymbol{b}$, one can determine the temperature dependence of the enhancement factor $\eta_y(T)$ for temperatures $T < T_{\mathrm{M}}$ using

$$H_p(\Gamma_1 \leftrightarrow \Gamma_4) = \sqrt{\frac{2\left(K_2^{ab} + K_4^{ab}\right)}{\chi_\perp\left(1+\eta_y\right)^2}}. \tag{28}$$

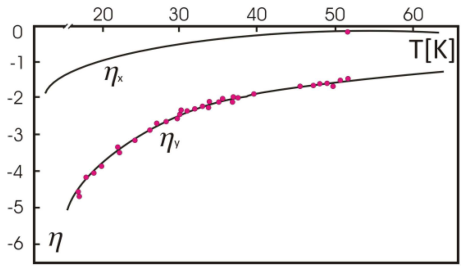

Fig. 21. Temperature dependencies of the enhancement coefficients η_x and η_y in $DyFeO_3$. The plotted curves correspond to the relations $\eta_x = -24.9/T$, $\eta_y = -74.6/T$, respectively.

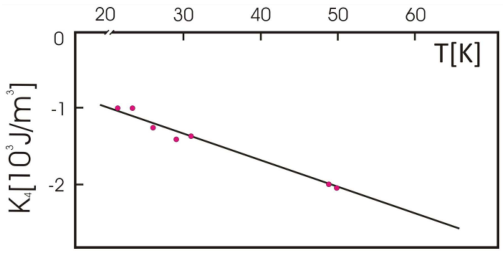

Fig. 22. Temperature dependence of the fourth-order anisotropy constant K_4 in $DyFeO_3$.

In the considered case, it is possible to determine the dependence describing the instability fields for the antiferromagnetic and ferromagnetic phases. The dependence $\eta_y(T)$ is presented in Fig. 21. According to the theory [4], the temperature dependence of the enhancement coefficient $\eta_\alpha(T)$ is described by the following relation

$$\eta_\alpha = \frac{a}{M_0}\left(\frac{\mu_B^2 g_\alpha^2}{4T} + \chi_{VF}^{\alpha\alpha}\right), \tag{29}$$

where:

a — exchange constant,

M_0 — sublattice magnetization,

μ_B — Bohr magneton,

g_α — component of the gyromagnetic ratio of the Dy^{3+} ion, and

$\chi_{VF}^{\alpha\alpha}$ — van Vleck contribution to the magnetic susceptibility.

The obtained dependence $\eta_y(T)$ exhibits behavior of the type $\eta_y = \frac{C_y}{T}$, because the van Vleck contribution is independent of temperature and small compared to the temperature-dependent component. The constant C_y corresponding to the curve shown in Fig. 21 has the value $C_y = -74.6$. The excellent agreement between the experimental and theoretical dependencies allows one to conclude that this description $\eta_y = \frac{C_y}{T}$ can be applied in the temperature range $T_M < T < T_{cr}$.

Such good agreement between the $\eta_y(T)$ course determined from experimental data and the theoretical expression also permits the use of (29) to determine the enhancement coefficient $\eta_x(T)$. According to theretical calculations, the temperature-dependent coefficients η_x and η_y, determined by the paramagnetic susceptibility, yield a ratio that is equal to the square of the ratio of the respective components of the gyromagnetic factor,

$$\frac{\eta_x}{\eta_y} = \frac{g_x^2}{g_y^2}. \tag{30}$$

Based on (30), one can obtain the value $C_x = -24.9$ using the values of $g_x = 10$ and $g_y = 17.3$ [4, 48]. To calculate the van Vleck contribution to η_x, one can use the condition $\tan(\alpha^*) = \pm(1+\eta_x)(1+\eta_y)$ that holds at the Morin temperature T_M, employing the experimentally determined critical angle $\alpha^* \approx 62°$ for dysprosium orthoferrite. Solving the resulting equation leads to two possible values, namely $C_{x0}^{(1)} = 0.32$ and $C_{x0}^{(2)} = -1.39$. A comparison between the experimental phase diagrams in oblique fields and the theoretical predictions indicates better agreement for the value $C_{x0}^{(1)} = 0.32$.

Figure 21 shows the temperature dependence of $\eta_x(T)$ calculated from

$$\eta_x(T) = \frac{C_x}{T} + C_{x0}, \tag{31}$$

using the values $C_x = -24.9$ and $C_{x0} = 0.32$.

The enhancement coefficient η_z can be assumed to be zero, as the component g_z is very small [49]. As shown previously for $\eta_x(T)$ and $\eta_y(T)$, the van Vleck contribution to η_z is also negligibly small.

In calculations of phase diagrams for $DyFeO_3$ in oblique magnetic fields, the fourth-order anisotropy constant K_4^{bc} can also be assumed to be zero, considering the condition $K_4^{bc} \ll K_2^{bc}$. This approach allows the use of a thermodynamic potential in the form given by (4), where the only missing parameter is the fourth-order anisotropy constant K_4. This constant can be determined by numerically fitting experimental data on the temperature dependence of the phase transition field $H_p(\Gamma'_{1234} \leftrightarrow \Gamma''_{1234})$ for the external magnetic field $\boldsymbol{H}$ oriented in the crystallographic ab plane. The method involves adjusting K_4 to achieve the best agreement between the calculated and experimental values in the temperature range $T < T_M$, for various field orientation angles $\alpha > \alpha^*$. The determined values of $K_4(T)$ are shown in Fig. 22. By extrapolating the obtained linear dependence of $K_4(T)$ in the range $T > T_M$, one can obtain results that can be used in calculation in the range $T_M < T < T_{cr}$.

4.5.3. Summary — phase diagram calculations and equilibrium magnetic state parameters

Figures 16, 17, and 18 present phase diagrams for $DyFeO_3$ in oblique magnetic fields. In these diagrams, points represent experimental

data, while lines correspond to results obtained from calculations based on previously determined magnetic constants and phenomenological analysis. These lines represent phase transition fields as functions of temperature and the angle between the direction of the external magnetic field and a chosen crystallographic axis of the $DyFeO_3$ crystal.

The phase transition fields for the case $\boldsymbol{H} = (0, H_y, H_z)$ can also be calculated using the approximate formula (9). The results obtained with this equation are in very good agreement with both exact numerical results and experimental data.

As for the case $\boldsymbol{H} = (H_x, H_y, 0)$, using the approximate formula (15) to determine the transition field dependence $H_p(\Gamma'_{1234} \leftrightarrow \Gamma''_{1234})(T)$ also yields good agreement with the exact calculations for fields $H \leq 20$ kOe near the Morin point.

The calculated and experimentally obtained phase diagrams (Figs. 20 and 21) show a high degree of consistency in the field orientations within the *ac* and *bc* planes of the $DyFeO_3$ crystal. However, slightly lower agreement is observed between the experimental points and the calculated lines for the field $\boldsymbol{H} = (H_x, 0, H_z)$ at angles in the range of $80° < \gamma < 90°$. This discrepancy may be due to increased measurement uncertainty, as a strong dependence of the transition field on the magnetic field orientation is observed in this range.

Using and analyzing the recorded domain structure images as functions of external magnetic field orientation and temperature, as well as constructing phase diagrams, enables a more complete analysis of spin reorientation in $DyFeO_3$. Knowing the angles $\varphi(H,T)$ and $\theta(H,T)$ allows one to trace the magnetic evolution of the crystal by analyzing the position of the antiferromagnetic vector $\boldsymbol{G}$ in space.

5. Conclusions

The main results presented in this work can be summarized as follows. All phase transitions described and analyzed are characterized by significant reconstruction of the domain structure. Antiferromagnetic, weak ferromagnetic, and mixed oblique phases observed in dysprosium orthoferrite at various temperatures and external magnetic fields can, in specific regions (defined by temperature, field strength, and orientation), coexist near magnetic phase transitions, forming complex magnetic domain structures.

The observed transitions are of both first- and second-order. For instance, the transition $\Gamma_1 \rightarrow \Gamma_{1234}$ is a second-order phase transition, whereas the $\Gamma_{1234} \rightarrow \Gamma_4$ transition is of the first order. The complex domain structure transformations occurring during these transitions suggest possible difficulties in utilizing such materials in devices that exploit spin switching phenomena.

The presented phase diagrams, derived from domain structure changes during and near phase transitions, show very good agreement with the results obtained from theoretical predictions.

Acknowledgments

The presented results are the outcome of research and analysis carried out jointly with R. Szymczak and S.L. Gnatchenko. Part of this work was published in collaboration and is cited in this paper.

References

[1] R.L. White, *J. Appl. Phys.* **40**, 1061 (1969).

[2] T. Yamaguchi, *J. Phys. Chem. Solids* **35**, 479, (1974).

[3] K.P. Biełow, A.K. Zwiezdin, A.M. Kadomcewa, R.Z. Lewitin, *Orientational transition in Rare Earth Magnetic System*, Moskwa Nauka, 1979 (in Russian).

[4] A.K. Zwiezdin, W.M. Matwiejew, A.A. Muchin, A.I. Popow, *Rare Earth Ions in Magnetically Ordered Crystals*, Moskwa Nauka, 1985, p. 294 (in Russian).

[5] H. Su, S. Zheng, N. Wang, G. Zhu, X. Ju, *Acta Phys. Sin.* **74**, 087801 (2025).

[6] D. Afanasiev, J.R. Hortensius, B.A. Ivanov, A. Sasani, E. Bousquet, Y.M. Blanter, R.V. Mikhaylovskiy, A.V. Kimel, A.D. Caviglia, *Nat. Mater.* **20**, 607 (2021).

[7] T.N. Stanislavchuc, Y. Wang, Y. Janssen, G.L. Carr, S.W. Cheong, A.A. Sirenko, *Phys. Rev. B* **93**, 094403 (2016).

[8] S. Cao, L. Chen, W. Zhao et al., *Sci. Rep.* **6**, 37529 (2016).

[9] D. Afanasiev, B.A. Ivanov, A. Kirilyuk, T. Rasing, R.V. Pisarev, A.V. Kimel, *Phys. Rev. Lett.* **116**, 097401 (2016).

[10] D. Afanasiev, A.K. Zvezdin, A.V. Kimel, *Opt. Express* **23**, 23978 (2015).

[11] T. Nakajima, Y. Tokunaga, Y. Toguchi, Y. Tokura, T. Arima, *Phys. Rev. Lett.* **115**, 197205 (2015).

[12] Y. Tokunaga, S. Iguchi, T. Arima, Y. Tokura, *Phys. Rev. Lett.* **101**, 097205 (2008).

[13] E.F. Bertaut, *Magnetism*, Vol. 3, Academic Press, New York 1963.

[14] A. Maziewski, R. Szymczak, *J. Phys. D Appl. Phys.* **10**, L37 (1977).

[15] N.F. Kharchenko, R. Szymczak, V.V. Eremenko, S.L. Gnatchenko, H. Szymczak, *Solid State Commun.* **22**, 463 (1977).

[16] S.L. Gnatchenko, N.F. Kharchenko, R. Szymczak, *Izv. Akad. Nauk SSSR Ser. Fiz.* **44**, 1461 (1980).

[17] K. Piotrowski, A. Szewczyk, R. Szymczak, V.V. Eremenko, S.L. Gnatchenko, N.F.Kharchenko, *Acta Phys. Pol. A* **68**, 139 (1985).

[18] A.V. Zalessky, A.M. Savvinov, I.S.Zheludev, A.N. Ivashchenko, *Sov. Zh. Eksp. Teor. Fiz. (JETP)* **68**, 1449 (1975).

[19] S.L. Gnatchenko, K. Piotrowski, R. Szymczak, *Sov. Low Temp. Phys.* **19**, 552 (1993).

[20] S.L. Gnatchenko, K. Piotrowski, A. Szewczyk, R. Szymczak, H. Szymczak, *J. Magn. Magn. Mater.* **128**, 307 (1994).

[21] S.L. Gnatchenko, K. Piotrowski, R. Szymczak, H. Szymczak, *J. Magn. Magn. Mater.* **140–144**, 2163 (1995).

[22] V.V. Eremenko, S.L. Gnatchenko, N.F. Kharchenko, P.P. Lebedev, K. Piotrowski, H. Szymczak, R. Szymczak, *Europhys. Lett.* **11**, 1327 (1987).

[23] E.A. Turov, *Physical Properties of Magnetically Ordered Crystals*, Academy of Sciences of USRR, 1963 (in Russian).

[24] A.I. Mitsek, N.P. Kolmacova, *Fiz. Met. Metalloved.* **22**, 161 (1966).

[25] V.V. Eremenko, S.L. Gnatchenko, N.F. Kharchenko, P.P. Lebedev, K. Piotrowski, *J. Phys.* **49**, C8-919 (1988).

[26] S.L. Gnatchenko, N.F. Kharchenko, P.P. Lebedev, K. Piotrowski, H. Szymczak, R. Szymczak, *J. Magn. Magn. Mater.* **81**, 125 (1989).

[27] S.L. Gnatchenko, P.P. Lebedev, K. Piotrowski, N.F. Kharchenko, R. Szymczak, in: *17th All-Union Conf. on Physics of Magnetic Phenomena, Kalinin*, 1988 p. 754.

[28] S. Kurita, Y. Tazaka, K. Tsushima, *J. Phys. Soc. Jap.* **56**, 612 (1987).

[29] K. Piotrowski, R. Szymczak, H. Szymczak, V.V. Eremenko, S.L. Gnatchenko, N.F.Kharchenko, P.P. Lebedev, *IEEE Trans. Magn.* **24**, 1701 (1988).

[30] S.L. Gnatchenko, P.P. Lebiediev, N.F. Charchenko, K. Piotrowski, R. Szymczak, *Sov. Low Temp. Phys.* **15**, 868 (1989).

[31] S.L. Gnatchenko, N.F. Charchenko, K. Piotrowski, H. Szymczak, R. Szymczak, *Zh. Eksp. Teor. Fiz.* **99**, 874 (1991).

[32] A.I. Micek, N.P. Kaumakowa, *Fiz. Mag. Mat.* **22**, 161 (1966).

[33] A.I. Mitsek, N.P. Kaumakowa, *Phys. Status Solidi B* **25**, 787 (1968).

[34] O.G. Miedwiedowskaja, G.K. Czienurnik, *Sov. Fiz. Tw. Tieła* **27**, 3144 (1985).

[35] O.G. Miedwiedowskaja, G.K. Czienurnik, *Sov. Fiz. Tw. Tieła* **28**, 3203 (1986).

[36] A.N. Bałganow, A.W. Żurawlew, A.I. Puzynia, *Low Temp. Phys.* **15**, 181 (1989).

[37] W.G. Bariachtar, A.N. Bogdanow, D.A. Jabłonskij, *Sov. Usp. Fiz. Nauk* **156**, 47 (1988).

[38] A. Hubert, *Tieoria Domennych Stienok w Yporiadoczennych Sriedach*, Mir, Moskwa 1977, p. 306.

[39] E.M. Lifszyc, *Zh. Eksp. Teor. Fiz. (JETP)* **15**, 97 (1945).

[40] A. Hubert, *Phys. Status. Solidi B* **22**, 709 (1967).

[41] A.A. Halfina, M.A. Szamsutdinow, M.M. Farztdinow, *Fiz. Mag. Mat.* **61**, 820 (1986).

[42] M.A. Szamsutdinow, A.A. Halfina, M.M. Farztdinow, *Fiz. Mag. Mat.* **65**, 22 (1990).

[43] W.G. Bariachtar, A.N. Bogdanow, D.A. Jabłonskij, *Sov. Fiz. Tw. Tieła* **28**, 3333 (1986).

[44] A.K. Zwiezdin, I.A. Zorin, A.M. Kadomcewa, I.B. Krynieckij, A.S. Moskwin, A.A. Muchin, *Zh. Eksp. Teor. Fiz. (JETP)* **88**, 1098 (1985).

[45] D. Treves, *J. Appl. Phys.* **36**, 1033 (1965).

[46] A.K. Zwiezdin, W.M. Matwiejew, *Zh. Eksp. Teor. Fiz. (JETP)* **77**, 1076 (1979).

[47] H. Schuchert, S. Hufner, R. Faulhaber, *Z. Phys.* **220**, 273 (1969).

[48] G. Gorodetsky, B. Sharon, S. Strikman, *J. Appl. Phys.* **39**, 1371 (1968).

[49] N.F. Charchenko, S.L. Gnatchenko, R. Szymczak, *Acta Phys. Pol. A* **68**, 347 (1985).